iScience

Article

High-throughput screening identifies broad-spectrum Coronavirus entry inhibitors

High-throughput screening identifies Coronavirus entry inhibitors post-receptor binding

Pseudovirus Used	Assay Tier	Number of Compounds	
VSVΔG - Wuhan Spike	Primary Screen	~200,000 / 733	Putative inhibitors
VSVΔG - VSVG	Secondary Screen	65	Spike-specific entry inhibitors
VSVΔG - MERS Spike	Tertiary Screen	5	Entry inhibitors downstream of receptor binding

Identified broad-spectrum inhibitors:

PCM-0282478
(Unreported compound)

Chiral Separation →

PCM-0296174
(active enantiomer)

Suman Khan, Efrat Ozer Partuk, Jeanne Chiaravalli, ..., Fabrice Agou, Haim Michael Barr, Ori Avinoam

ori.avinoam@weizmann.ac.il

Highlights

High-throughput screening platform for coronavirus entry inhibitors

Tiered screen of 2×10^5 compounds identifies hits downstream of receptor binding

5 previously unreported validated hits

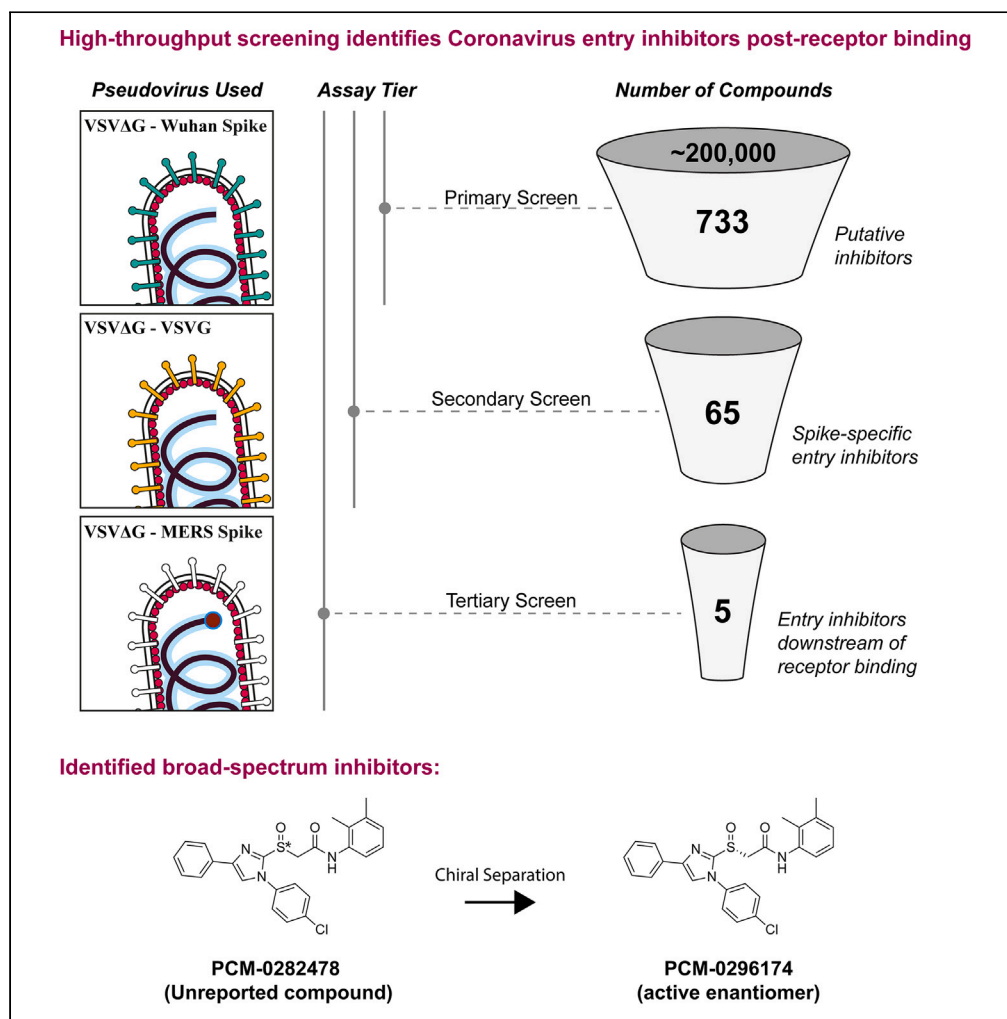1 broad-spectrum coronavirus entry inhibitor and its derivative discovered

Article

High-throughput screening identifies broad-spectrum Coronavirus entry inhibitors

Suman Khan,[1] Efrat Ozer Partuk,[1] Jeanne Chiaravalli,[2] Noga Kozer,[3] Khriesto A. Shurrush,[3] Yael Elbaz-Alon,[1] Nadav Scher,[1] Emilie Giraud,[2] Jaouen Tran-Rajau,[2] Fabrice Agou,[2] Haim Michael Barr,[3] and Ori Avinoam[1,4,*]

SUMMARY

The COVID-19 pandemic highlighted the need for antivirals against emerging coronaviruses (CoV). Inhibiting spike (S) glycoprotein-mediated viral entry is a promising strategy. To identify small molecule inhibitors that block entry downstream of receptor binding, we established a high-throughput screening (HTS) platform based on pseudoviruses. We employed a three-step process to screen nearly 200,000 small molecules. First, we identified hits that inhibit pseudoviruses bearing the SARS-CoV-2 S glycoprotein. Counter-screening against pseudoviruses with the vesicular stomatitis virus glycoprotein (VSV-G), yielded sixty-five SARS-CoV-2 S-specific inhibitors. These were further tested against pseudoviruses bearing the MERS-CoV S glycoprotein, which uses a different receptor. Out of these, five compounds, which included the known broad-spectrum inhibitor Nafamostat, were subjected to further validation and tested against pseudoviruses bearing the S glycoprotein of the Alpha, Delta, and Omicron variants as well as *bona fide* SARS-CoV-2. This rigorous approach revealed an unreported inhibitor and its derivative as potential broad-spectrum antivirals.

INTRODUCTION

Coronaviruses (CoVs) have garnered global attention due to their potential for causing severe diseases in humans. The most notable among these are SARS-CoV, MERS-CoV, and SARS-CoV-2, each responsible for significant disease outbreaks.[1] As zoonotic pathogens, CoVs continue to pose a constant threat to global health due to the potential for cross-species transmission, underscoring the need for broad-spectrum antiviral inhibitors.

The viral spike (S) glycoprotein of CoVs mediates fusion of the viral envelope with the host cell membrane, which is essential for infection and delivery of the viral genetic material into host cells.[2–4] This process is conserved across all coronaviruses, positioning the S glycoprotein as a promising target for broad-spectrum antiviral strategies.[5,6] The S glycoprotein is a class I viral fusogens, comprised of two subunits: S1, involved in host cell recognition and binding, and S2, which mediates membrane fusion.[3,7]

Current therapies for CoV infection largely aim to disrupt the S1 domain-mediated host recognition.[8] However, these strategies face significant limitations, particularly with the emergence of SARS-CoV-2 variants carrying mutations in the S1 domain that enhance receptor binding and facilitate immune evasion.[9–12] Additionally, the variability in the cellular receptors recognized by different CoVs presents a challenge for achieving broad inhibition with S1 domain-targeted strategies. For instance, SARS-CoV and SARS-CoV-2 recognize angiotensin-converting enzyme 2 (ACE2),[13,14] while MERS-CoV interacts with dipeptidylpeptidase 4 (DPP4).[15] Further, the identification of other SARS-CoV-2 receptors, such as TMEM106B[16] highlights the adaptability of CoVs in exploring alternative receptors.

Strategies to inhibit host proteases like transmembrane protease serine 2 (TMPRSS2)[17–19] and cathepsins,[20,21] which facilitate CoV entry by cleaving the S protein and activating the fusogenic activity of the S2 domain, have also been explored. Protease inhibitors like nafamostat[22] and camostat[19] have demonstrated some efficacy against multiple CoVs.[23,24] However, their inhibition spectrum remains uncertain due to the adaptability of CoVs in exploring alternative proteases,[25] and their evolution to include a polybasic furin cleavage site,[26,27] thereby limiting the strategy of targeting a single protease for broad-spectrum inhibition.

In contrast, the S2 domain presents as a promising target for managing CoV infection. Cross-reactive neutralizing antibodies (nAbs) against the S2 domain have been identified in individuals who have not contracted SARS-CoV-2, as well as patients infected with various CoVs.[28,29] This compelling evidence is reinforced by the essential role of the S2 domain in the universally conserved biophysical process of membrane fusion. Additionally, in comparison to the S1 domain, the S2 domain has exhibited lower mutation rates in emerging SARS-CoV-2 variants, which is further supported by phylogenetic analyses showing a higher degree of sequence conservation in the S2

[1]Department of Biomolecular Sciences, Weizmann Institute of Science, Rehovot 7610001, Israel
[2]Institut Pasteur, Université Paris Cité, CNRS UMR 3523, Chemogenomic and Biological Screening Core Facility, C2RT, Paris, France
[3]The Wohl Drug Discovery Institute of the Nancy and Stephen Grand Israel National Center for Personalized Medicine, Weizmann Institute of Science, Rehovot 7610001, Israel
[4]Lead contact
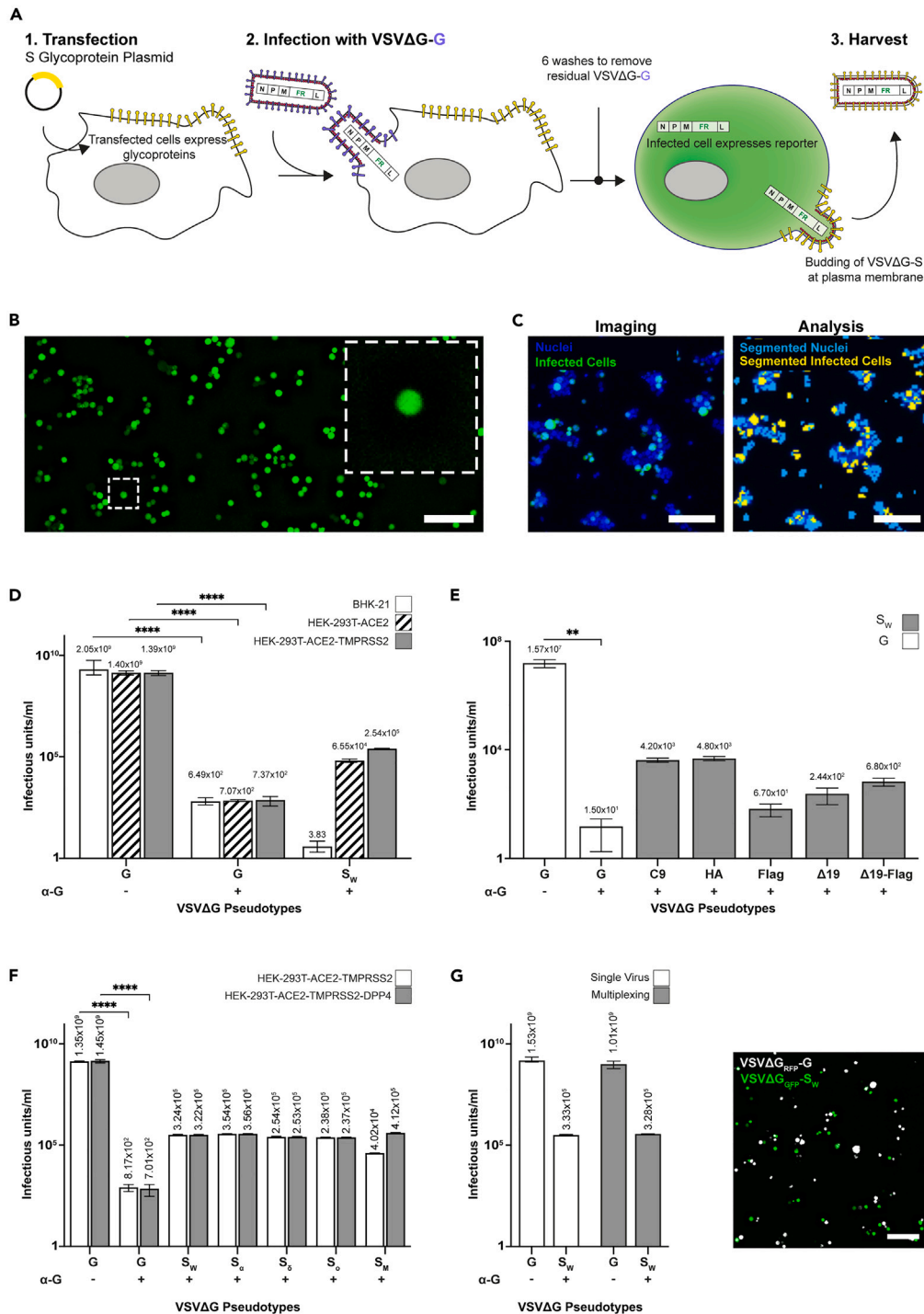*Correspondence: ori.avinoam@weizmann.ac.il
https://doi.org/10.1016/j.isci.2024.110019

A

1. Transfection
S Glycoprotein Plasmid

Transfected cells express glycoproteins

2. Infection with VSVΔG-G

6 washes to remove residual VSVΔG-G

Infected cell expresses reporter

3. Harvest

Budding of VSVΔG-S at plasma membrane

B

C

Imaging
Nuclei
Infected Cells

Analysis
Segmented Nuclei
Segmented Infected Cells

D

BHK-21
HEK-293T-ACE2
HEK-293T-ACE2-TMPRSS2

****

Infectious units/ml

2.05×10^9 1.39×10^9
1.40×10^9

6.49×10^2 7.37×10^2
7.07×10^2

6.55×10^4 2.54×10^5

3.83

α-G   −   +   +
VSVΔG Pseudotypes: G   G S_W

E

S_W
G

**

1.57×10^7

4.20×10^3 4.80×10^3

1.50×10^1 6.70×10^1 2.44×10^2 6.80×10^2

Infectious units/ml

α-G   −   +   +   +   +   +   +
VSVΔG Pseudotypes: G   G   C9   HA   Flag   Δ19   Δ19-Flag

F

HEK-293T-ACE2-TMPRSS2
HEK-293T-ACE2-TMPRSS2-DPP4

**** ****

1.35×10^9 1.45×10^9

3.24×10^5 3.22×10^5 3.54×10^5 3.56×10^5 2.54×10^5 2.53×10^5 2.38×10^5 2.37×10^5 4.12×10^5

8.17×10^2 7.01×10^2

4.02×10^4

Infectious units/ml

α-G   −   +   +   +   +   +
VSVΔG Pseudotypes: G   G S_W $S_α$ $S_δ$ S_o S_M

G

Single Virus
Multiplexing

1.53×10^9 1.01×10^9

3.33×10^5 3.28×10^5

Infectious units/ml

α-G   −   +   −   +
VSVΔG Pseudotypes: G S_W G S_W

VSVΔG$_{RFP}$-G
VSVΔG$_{GFP}$-S_W

Figure 1. Production of high titer VSVΔG pseudoviruses and quantification of single infection events

(A) A schematic representation of the VSVΔG pseudoviruses production process. Viral glycoproteins (yellow) are expressed by plasmid transfection on cell surface. Transfected cells are subsequently infected with recombinant VSV in which the endogenous G glycoprotein (VSV-G) was replaced with a fluorescent reporter (VSVΔG) and complemented with VSV-G (VSVΔG-G). 1 h post-infection, the residual VSVΔG-G is thoroughly washed and the culture is replenished with medium. This results in the production of pseudovirus particles capable of a single round of infection, baring the desired glycoproteins on their surface. Nevertheless, all downstream experiments are performed in the presence of a neutralizing anti-VSV-G antibody (α-G). (B) A widefield image of cells infected with VSVΔG pseudoviruses expressing a fluorescent reporter (GFP; green). Infected cells become round after infection due to the virus-induced cytopathic effect (CPE).

Figure 1. Continued

(C) (Left) A high magnification overlay image showing the infected GFP-positive cells (green) and nuclei (blue). (Right) The respective segmentation showing infected cells (yellow) and nuclei (cyan).

(D–F) Pseudoviral titers in infectious units/mL. To remove any residual infections from VSVΔG-G, the neutralizing α-G antibody was added to all pseudoviruses, ensuring accurate titration. The activity of α-G was tested using VSVΔG-G in the presence and absence of α-G. Two-tailed unpaired t tests were used to evaluate the statistical significance of α-G activity (p ** ≤ 0.01, **** ≤ 0.0001. $N_{experiments}$ = 3, $n_{repeats}$ = 9. (D) Titer of VSVΔG-S_W in different cell types showing infection improves upon over-expression of the innate receptor ACE2 and host protease TMPRSS2. (E) Titer of VSVΔG-S_W in HEK-293T-ACE2-TMPRSS2 cells showing the effect of modifications to the cytosolic tail of S_W. (F) Titer of VSVΔG-G, Wuhan (S_W), Alpha ($S_α$), Delta ($S_δ$), Omicron (S_o), and MERS-CoV S (S_M) showing similar infection levels, with and without DPP4. VSVΔG-G pseudoviruses infected all cell lines at similar levels (D and F).

(G) Pseudoviral infectious units/mL of VSVΔG_{RFP}-G and VSVΔG_{GFP}-S_W separately or simultaneously result in equivalent titer measurements. (Right) A high magnification overlay image of a well showing VSVΔG_{RFP}-G and VSVΔG_{GFP}-S_W infected cells (white and green, respectively). Scale bar is 100 μM (B, C, and G). Error bars represent the SEM.

domains of diverse CoV clades.[12,30–33] These characteristics of the S2 domain suggest its potential as a broad-spectrum therapeutic target. However, targeting the S2 domain is challenging because it cannot be expressed independently of the S1 domain. Hence, current FDA-approved drugs for treating COVID-19 patients, such as Remdesivir,[34] Molnupiravir,[35] and Nirmatrelvir,[36] do not specifically target the S2 domain.

High-throughput screening (HTS) has been used to identify antiviral leads for various viruses.[37–39] With the emergence of SARS-CoV-2, several HTS assays were swiftly developed, predominately focusing on FDA-approved drugs, to reduce the development time by re-purposing existing drugs.[40–44] Despite numerous efforts, few efficient antivirals were identified.[45–49] Furthermore, while numerous *in silico* and *in vitro* HTS approaches targeting viral entry or viral replication have been developed, efforts specifically dedicated to the identification of broad-spectrum CoV antivirals through HTS have been sparse.[50,51]

To address this gap, we adopted a pseudotyped vesicular stomatitis virus (VSV) model[52] that permitted robust quantification of CoV spike glycoprotein mediated infection. We established an HTS platform and screened approximately 200,000 diverse chemical compounds. We targeted the S2 domain of the S glycoproteins by screening against the glycoproteins of two distinct CoVs that bind different cellular receptors.[30,53–55] Our extensive HTS efforts resulted in the identification and validation of a previously unreported broad-spectrum antiviral compound.

RESULTS

Pseudoviruses expressing fluorescent reporters enable robust infection quantification

To develop an effective high-throughput screening (HTS) assay for SARS-CoV-2, we produced pseudoviruses featuring the S glycoprotein of the SARS-CoV-2 Wuhan variant (VSVΔG-S_W) on a VSV backbone lacking VSV-G (VSVΔG) (Figure 1A). We chose to work with VSVΔG which expresses a fluorescent reporter from the viral genome after infection (Figure 1B). We employed a fluorescent reporter, instead of the more commonly used luciferase, because it allows direct visualization and robust quantification of single infection events, overcoming the need for averaging and the additional processing steps for the luciferase enzymatic reaction[56] (Figure 1C).

We confirmed the tropism of the VSVΔG-S_W pseudoviruses by comparing infected ACE2-overexpressing human embryonic kidney (HEK-293T-ACE2) cells and ACE-2-deficient baby hamster Kidney (BHK-21) cells (Figure 1D). To eliminate potential residual infections from VSVΔG-G that might have been left over during production, we performed all experiments in the presence of a neutralizing antibody against VSV-G. We observed 10,000-fold more infections in HEK-293T-ACE2, with an additional 3.8-fold increase in cells co-expressing TMPRSS2 (HEK-293T-ACE2-TMPRSS2), consistent with the tropism of SARS-CoV-2 (Figure 1D).

We then explored methods to enhance virus titers, comparing modifications to the cytosolic tail of the S glycoprotein and optimizing the production and infection procedures (Figures 1E, S1A, and S1B). Modifications included truncating the 19-amino acid ER retention sequence[57,58] and adding an HA, flag, or C9 tag to the C-terminus of the S glycoprotein.[19,59] Optimal titers were achieved with C9- and HA-tagged S glycoproteins without further modifications (Figure 1E). Moreover, we obtained peak titers when the cell supernatant containing VSVΔG-S_W was harvested 30 h after infection with the VSVΔG-G helper virus. Notably, infection rates doubled when cultures were centrifuged post-infection (Figures S1A and S1B). These optimizations significantly improved the sensitivity and reproducibility of infection counts.

Subsequently, we produced and obtained high titer pseudoviruses featuring the S glycoproteins of MERS-CoV (VSVΔG-S_M) and SARS-CoV-2 variants Alpha (VSVΔG-$S_α$), Delta (VSVΔG-$S_δ$), and Omicron (VSVΔG-S_o) and quantified infection rates in both HEK-293T-ACE2-TMPRSS2-DPP4 and HEK-293T-ACE2-TMPRSS2 cell lines (Figure 1F). Importantly, we assessed the infection rates of VSVΔG pseudoviruses expressing either GFP or RFP and featuring the S glycoprotein (VSVΔG_{GFP}-S_W) or VSV-G (VSVΔG_{RFP}-G), respectively (Figure 1G). Our results showed that comparable titers were achieved in both single and multiplexed infections, demonstrating the feasibility of multiplexing the assay using pseudoviruses expressing different fluorophores (Figure 1G).

Optimization and validation of a high-throughput screening assay for infection inhibitors

Building on the robust segmentation and quantification capabilities of our automated imaging system and the fluorescence-based assay using VSVΔG pseudoviruses (Figures 1B and 1C), we tailored the assay for high-throughput screening (HTS) in a 384-well format (Figure 2A). To streamline the plating process and ensure robust and reproducible quantification, compounds in DMSO were pre-plated in 384-well plates.
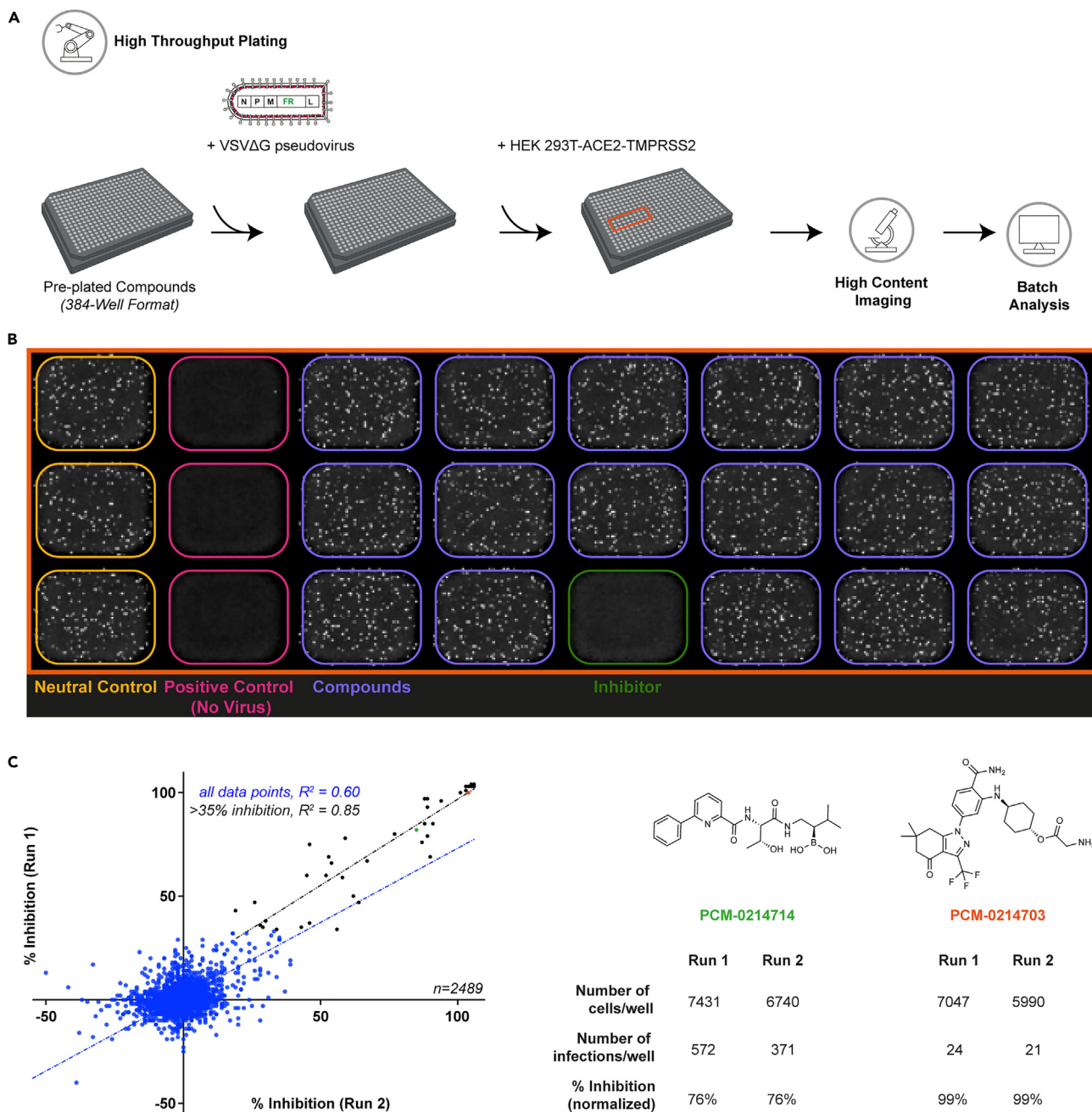
Figure 2. The pseudovirus-based HTS platform demonstrates high reproducibility

(A) Schematic of the high content screening pipeline: plating, imaging, and analysis. Compounds were pre-plated, and pseudoviruses, pre-incubated with α-G to neutralize any residual VSVΔG-G infection, were added in individual wells before introducing HEK-293T cells stably overexpressing SARS-CoV-2 receptor ACE2 and protease TMPRSS2. After 24 h, the nuclei were stained, and the plates were imaged. Images were subsequently segmented and quantified. (B) Overview image of a portion of a 384-well screening plate (orange box in A). The neutral control (yellow wells) indicates 100% infection, and the positive control (magenta wells) signifies 0% infection or 100% inhibition. The green well depicts an example of a compound with ~90% inhibition.

(C) Scatterplot of 2,489 compounds tested as single point, on two different days. Blue line is the fit for the compounds that inhibited >35%. The inhibitions were reproducible with a high correlation fit ($R^2 = 0.85$). Black line represents the fit for the rest of the compounds ($R^2 = 0.60$). (Right) Examples of two inhibitors showing similar inhibition values after normalization and despite having different total cell and infection counts.

Then, 10 μL of a pseudovirus suspension that contained between 500 and 1,000 infectious units, due to variations in production, was added to each well. Subsequently, 10,000 HEK-293T-ACE2-TMPRSS2 cells were added to each well and the plates were centrifuged and incubated for 24 h (Figure 2A).

After infection, the nuclei were stained to estimate cell count. Automated HTS imaging was then used to obtain images of the infected cells and nuclei in each well. These images were automatically segmented and analyzed by a dedicated pipeline (Figures 1C and 2B). The first columns of each plate, which contained viruses and cells, were used as a neutral control, providing the baselines for the infection and cell number counts (Figures 2B and S2). The raw infection and cell number counts from each well were normalized with the geometric means of the infection and cell number counts in the neutral control to determine the baselines for the inhibition and cytotoxicity profiles for each compound (Figures 2B and S2). The second columns contained only cells and served as the baseline for 0% infection as the geometric mean of counts in these wells, which also served as the positive controls (Figures 2B and S2). For consistency, all wells without compounds were supplemented with DMSO to achieve a final concentration of 0.1%.

To test the reproducibility of the assay and ascertain if a one-time screen at a single concentration for each compound would be likely to identify putative inhibitors, we ran a pilot screen with a subset of 2,489 compounds, approximately 1.25% of the entire compound library (Figure 2C). Each compound was assessed at a concentration of 10 μM for its ability to inhibit VSVΔG-S_W in two separate experiments. Compounds were reliably detected with similar inhibition levels ($R^2 = 0.60$), independent of day-to-day variations, regardless of the number of cells or the raw infection counts (Figure 2C), confirming the robustness of the assay, with Z′ factors 0.66 ± 0.04 and 0.76 ± 0.07 for the respective runs. To set a cut-off threshold for the screen, we chose compounds showing at least 35% inhibition, as this level of inhibition showed high reproducibility in the pilot screen ($R^2 = 0.85$).

A three-tiered screen identifies CoV entry inhibitors downstream of receptor binding

To identify potential S2-domain-specific inhibitors, we divided our screening process into three distinct tiers (Figure 3A). The primary screen evaluated an extensive library of approximately 200,000 compounds against VSVΔG-S_W at a single concentration of 10 μM. This process identified 733 compounds capable of inhibiting VSVΔG-S_W infection by at least 35% while maintaining cell viability of 65% (Table S1). For the secondary screen, the 733 compounds were tested against VSVΔG-G to distinguish S_W-specific inhibitors from non-specific ones. Since VSVΔG-S_W and VSVΔG-G share the VSVΔG backbone and only differ in the surface glycoproteins, compounds inhibiting VSVΔG-S_W but not VSVΔG-G were deemed S_W-specific. The screening identified 65 spike-specific inhibitors that inhibited VSVΔG-S_W infection by at least 35% without inhibiting VSVΔG-G infection by more than 35% (Table S2).

Subsequently, these 65 compounds were subjected to a tertiary screen against VSVΔG-S_M, to differentiate them from receptor binding inhibitors. Since MERS-CoV utilizes DPP4 as its host receptor, compounds inhibiting both VSVΔG-S_W and VSVΔG-S_M likely act downstream of receptor binding. This screen yielded 22 such inhibitors that reduced VSVΔG-S_M infection by at least 35% (Table S3). Out of these, we chose the 11 most drug-like inhibitors that were previously unreported, and Nafamostat, a known TMPRSS2 protease inhibitor, which we used as a positive control in subsequent experiments.[22]

To evaluate the screening platform, we calculated HTS parameters such as Z′ factor, signal-to-background (S/B), and coefficient of variation (%CV) for 569 plates from all three screening levels[60] (Figure 3B). These showed the robust performance of the screening platform with a high Z′ factor (0.8 ± 0.09) and a very high S/B (10^3), suggesting excellent sensitivity and accuracy. In addition, the low %CV ($1.9 \pm 0.74\%$ for neutral controls and $0.1 \pm 0.03\%$ for positive control) indicates the high reproducibility and precision of the platform. Plates that failed to meet the accepted Z′ cut-off of 0.5 underwent manual checks for errors in the infection counts of the positive and negative controls, and any outlier wells were excluded before data normalization.

To ensure the reliability of the HTS platform and rule out potential false positives due to compound degradation of quality, we resourced 4 of the 11 previously unreported compounds (PCM-0068389, PCM-0166392, PCM-0179622, PCM-0163855; Table S3) and Nafamostat that were available from alternative vendors and reassessed their activity against VSVΔG-S_W VSVΔG-G, and VSVΔG-S_M, (Figures 3C and 3D). These compounds demonstrated varied inhibitory activity against VSVΔG-S_W (38%–87%) and VSVΔG-S_M (27%–94%) but did not significantly inhibit VSVΔG-G (−23%–0%) confirming their selectivity (Figure 3D).

Dose response and cytotoxicity of putative candidate compounds

Next, we evaluated the cytotoxicity (CC_{50}) and IC_{50} value for each compound using a concentration range of 0.3125–40 μM against VSVΔG-S_W, VSVΔG-G, and VSVΔG-S_M, as well as VSVΔG-S_α, VSVΔG-S_δ, and VSVΔG-S_o. Since the purity of these compounds ranged from 70% to 95% and as an additional validation step, we performed these experiments on the compounds before and after HPLC purification. All compounds showed low to moderate cytotoxicity before and after purification (Figures S3 and 4, respectively).

Nafamostat showed similar IC_{50} values against VSVΔG-S_W (0.90 μM vs. 1.31 μM) and VSVΔG-S_M (0.13 μM vs. 0.21 μM) before and after purification, with no significant activity against VSVΔG-G, and was also active against VSVΔG-S_α (0.92 μM vs. 0.93 μM), VSVΔG-S_δ (0.31 μM vs. 0.94 μM), and VSVΔG-S_o, but the latter only after purification (Not calculated vs. 1.81 μM) (Figures S3 and 4). PCM-0068389, while showing extremely promising activity and selectivity before purification, lost all activity against VSVΔG-S_W, its variants and VSVΔG-S_M after purification and showed some activity against VSVΔG-G at concentrations higher than 10 μM (Figures S3 and 4). PCM-0166392 and PCM-0179622 while retaining relatively high activity against VSVΔG-S_W and its variants were not selective against VSVΔG-S_M yielding dose-response curves that were not significantly different from VSVΔG-G (Figures S3 and 4).

PCM-0163855 retained high selectivity to VSVΔG-S_W (0.60 μM vs. 0.70 μM), VSVΔG-S_α (0.37 μM vs. 0.40 μM), and VSVΔG-S_δ (0.45 μM vs. 0.49 μM), with only moderate activity against VSVΔG-S_o (41.18 μM vs. 30.77 μM) but was inactive against VSVΔG-S_M, showing no significant difference from VSVΔG-G above 10 μM concentration (Figures S3 and 4). Consistently, PCM-0163855 inhibited the replication of *bona fide* SARS-CoV-2 Delta (B.1.617.2) in VeroE6 cells with and without TMPRSS2 overexpression (6.71 μM and 6.43 μM, respectively; Figure S4A).
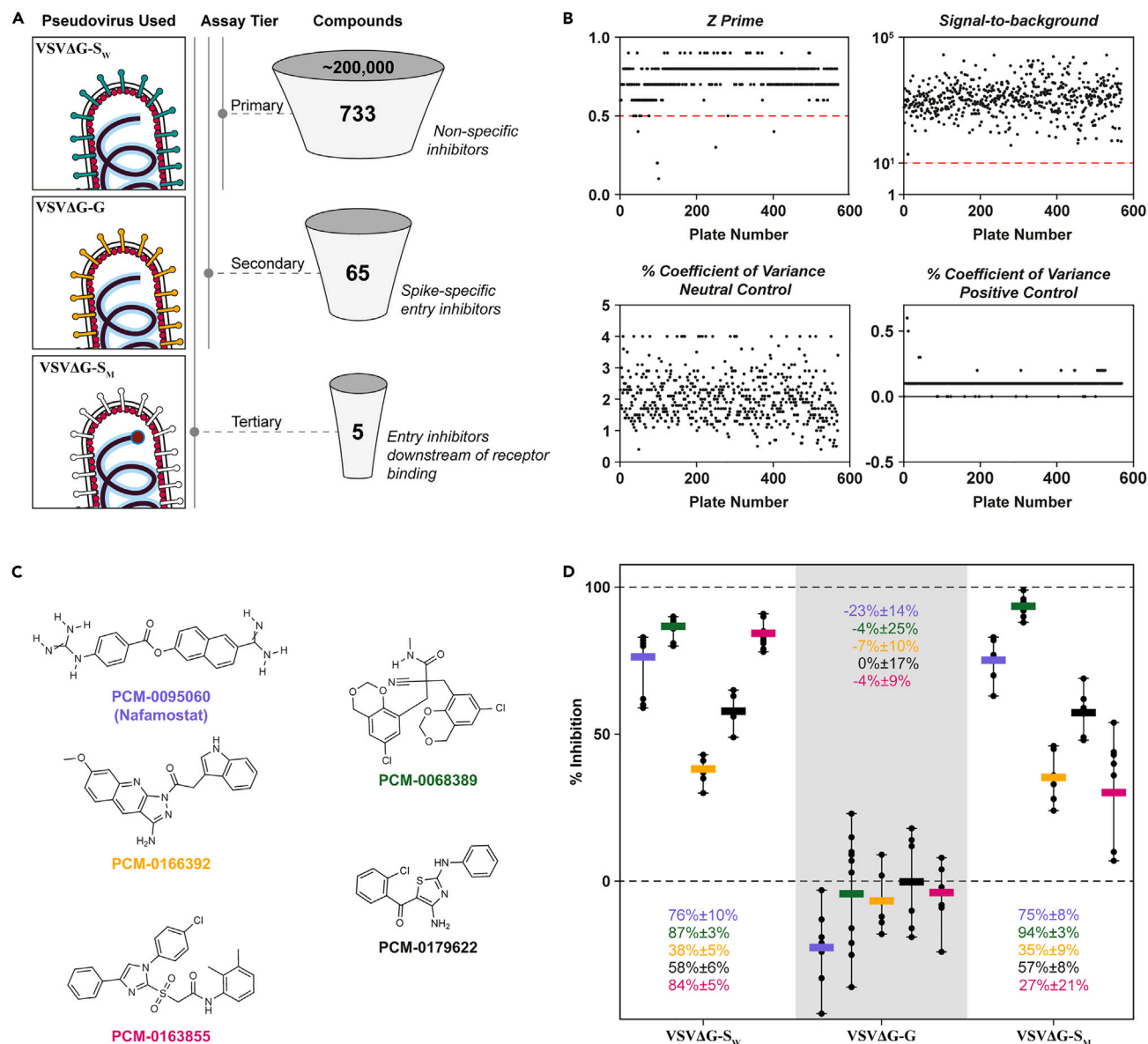
Figure 3. A three-tiered screen identifies putative entry inhibitors of CoVs

(A) Schematic showing primary screening of ~200,000 compounds against Wuhan SARS-CoV-2 Spike (VSVΔG-S_W) yielded 733 putative spike-specific and non-specific inhibitors. S_W specific inhibitors were identified by a secondary screen against VSV-G (VSVΔG-G) yielding 65 putative inhibitors. The tertiary screen with MERS-CoV spike (VSVΔG-S_M) and initial validation resulted in 5 compounds that were putatively broad-spectrum inhibitors.

(B) Plots showing HTS parameters to determine the robustness of our screen: Z′ factor, signal-to-background, percentage of coefficient of variance for positive and negative for the primary screen. Red line denotes the cut off for a robust plate. Five plates that failed to meet the cut-off for Z prime were manually checked for data quality.

(C) The chemical structures of the four previously unreported compounds and nafamostat that were commercially resourced.

(D) Plot of the inhibition of the resourced compounds against the three viruses. All the compounds selectively inhibit SARS-CoV-2 and MERS-CoV Spikes without inhibiting VSV-G. Error bars represent the range. Values represent mean inhibitions ± standard deviations.

A PCM-0163855 derivative is a broad-spectrum CoV inhibitor

Following up on these promising results, we synthesized PCM-0163855 and its sulfoxide derivative PCM-0282478 (Figure S5). We evaluated their IC$_{50}$ value against VSVΔG-$S_δ$, VSVΔG-S_o, VSVΔG-G, and VSVΔG-S_M, and *bona fide* SARS-CoV-2 variants, Delta (B.1.617.2), XBB.1.5, and CH.1.1 (Figures 5A and S6A). Dose-response curves demonstrated that PCM-0282478 was approximately 10 times more potent than synthesized PCM-0163855 against VSVΔG-$S_δ$ (1.13 μM and 14.40 μM, respectively) and selective against VSVΔG-S_o and VSVΔG-S_M (14.67 μM and
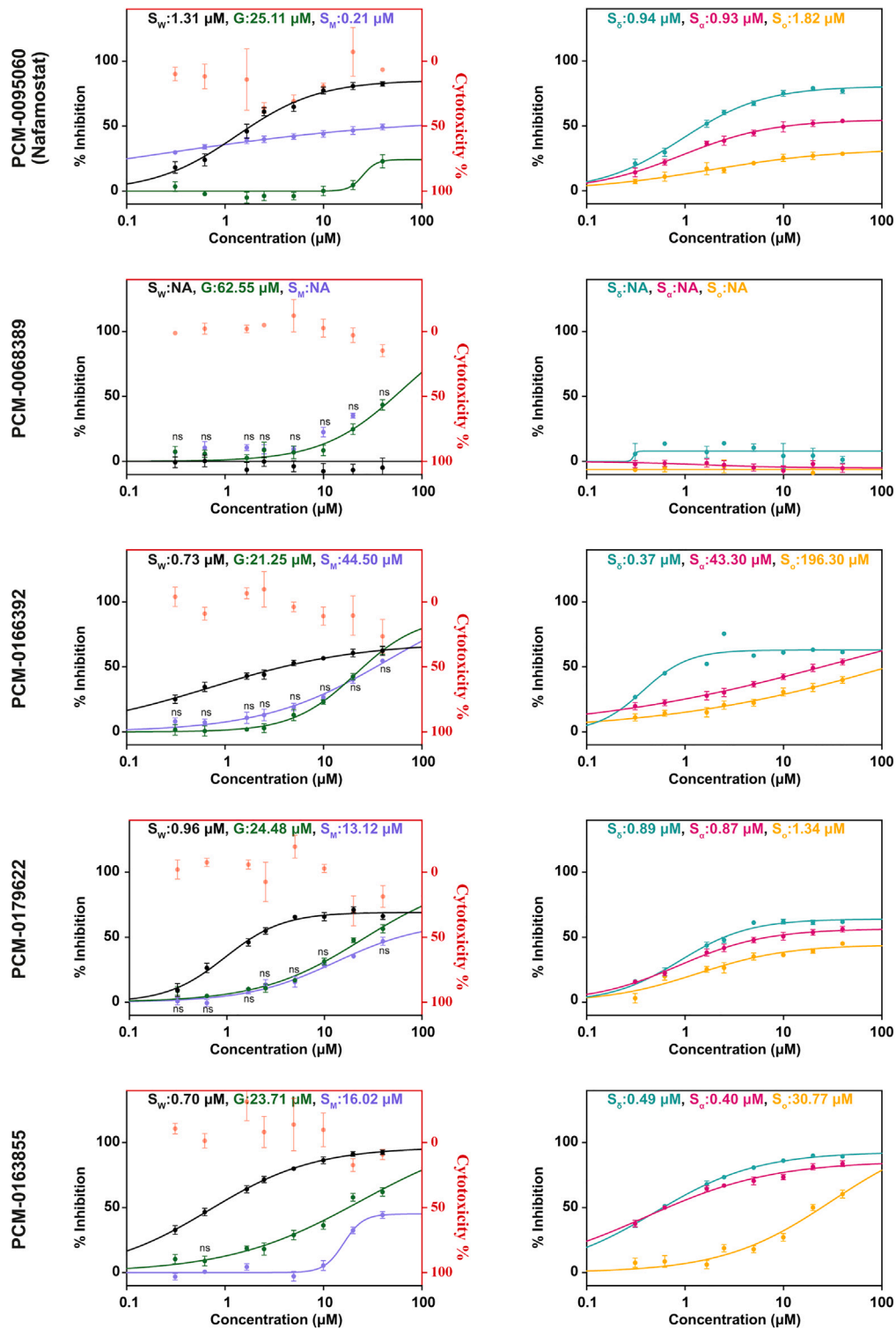
Figure 4. Dose-response activity and cytotoxicity of HPLC-purified compounds

(Left) Dose-response plot of the purified candidates against VSVΔG-S$_W$, VSVΔG-S$_M$, or VSVΔG-G and their cytotoxity profile.

(Right) Dose-response plots of hits against pseudoviruses with glycoproteins of SARS-CoV-2 variants (VSVΔG-S$_\alpha$: Alpha, VSVΔG-S$_\delta$: Delta, and VSVΔG-S$_o$: Omicron). Dose-response curve were fitted with a variable slope (four-parameter logistic model). Error bars represent the SEM. ns are the readings where there is no statistically significant difference between VSVΔG-SM and VSVΔG-G at a given concentration. For all other readings, the $p < 0.05$ (two-tailed unpaired t tests).
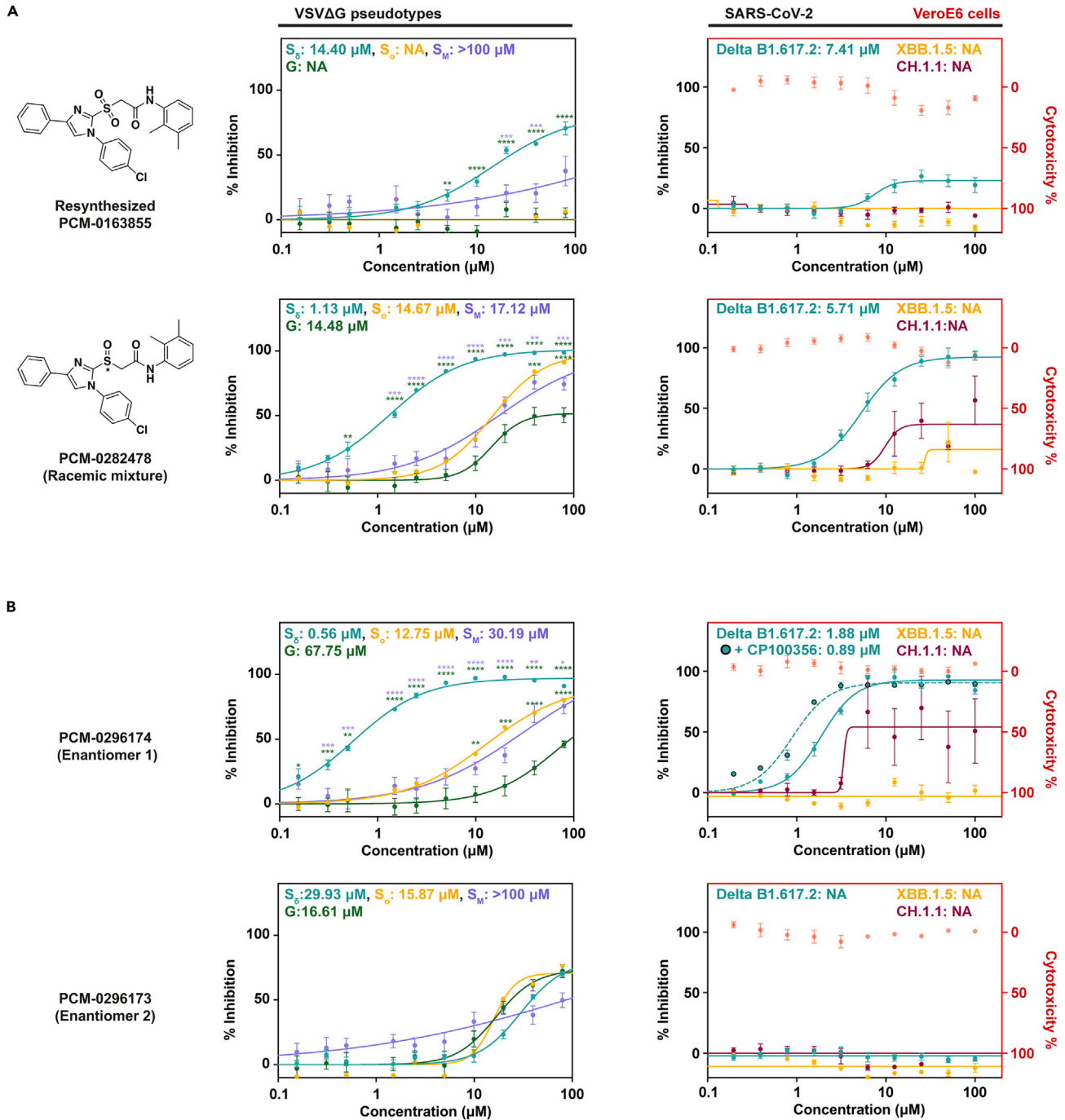
Figure 5. Validation of resynthesized PCM-0163855 and its sulfoxide derivatives

(A; Left) Structures of PCM-0163855 and its sulfoxide derivative PCM-0282478, and (Middle) corresponding dose-response plots comparing the inhibitory activity against VSVΔG-S$_\delta$, VSVΔG-S$_o$, VSVΔG-S$_M$ or VSVΔG-G, showing that PCM-0282478 exhibits a broader selectivity for inhibition compared to PCM-0163855, which was inactive against VSVΔG-G and, after resourcing, against VSVΔG-S$_M$ at all concentrations in pseudovirus based assay. (Right) The corresponding cytotoxicity profiles and dose-response plots comparing the inhibitory activity of *bona fide* SARS-CoV-2 variants, Delta B1.617.2, XBB.1.5, or CH.1.1, viral replication in Vero E6 cells.

(B; Left) Dose-response plots of two enantiomers of PCM-0282478 comparing the inhibitory activity against VSVΔG-S$_\delta$, VSVΔG-S$_o$, VSVΔG-S$_M$ or VSVΔG-G, showing that only one enantiomer exhibits a broader selectivity for inhibition in pseudovirus based assay. (Right) The corresponding cytotoxicity profiles and

Figure 5. *Continued*

dose-response plots comparing the inhibitory activity of *bona fide* SARS-CoV-2 variants. The active enantiomer, PCM-0296174 was also tested against Delta.B1.617.2 in presence of the multidrug resistance protein 1 (MDR1) inhibitor, CP100356. (A and B) Error bars represent the SEM. The statistical significance of the inhibitions was also determined. p * $\leq$ 0.05, ** $\leq$ 0.01, *** $\leq$ 0.001 **** $\leq$ 0.0001 (multiple unpaired t tests comparing group means, accounting for individual variance in each concentration and pseudovirus). $N_{experiments} \geq 2$, $n_{repeats} \geq 6$.

17.12 µM, respectively). Neither PCM-0163855 nor PCM-0282478 inhibited VSVΔG-G up to 10 µM. Furthermore, only PCM-0282478 inhibited *bona fide* SARS-CoV-2 Delta (B.1.617.2) replication in VeroE6 cells (4.49 µM; Figure 5A), and neither inhibited XBB.1.5 and CH.1.1 at the concentration range tested.

PCM-0282478 was synthesized as a racemic mixture. To evaluate the contribution of each enantiomer, we separated them to PCM-0296173 and PCM-0296174, and evaluated their IC_{50} value against VSVΔG-S$_\delta$, VSVΔG-S$_o$, VSVΔG-G, and VSVΔG-S$_M$ (Figure 5B). Only PCM-0296174 potently inhibited VSVΔG-S$_\delta$ and was selective against VSVΔG-S$_o$ and VSVΔG-S$_M$ (12.75 µM and 30.19 µM, respectively). The IC_{50} value of PCM-0296174 against VSVΔG-S$_\delta$ was approximately half compared to the racemic mixture PCM-0282478 (0.56 µM vs. 1.13 µM, respectively), showing a 2-fold increase in potency. Both PCM-0296173 and PCM-0296174 did not inhibit VSVΔG-G up to 10 µM. Further, only PCM-0296174 inhibited SARS-CoV-2 Delta (B.1.617.2) replication, and its IC_{50} improved by 2-folds in presence of an inhibitor against the multidrug resistance protein 1 (MDR1) efflux transporter (1.88 µM vs. 0.89 µM, respectively; Figure 5B). Conversely, PCM-0296174 inconsistently inhibited the Omicron variant CH.1.1 and did not inhibit XBB.1.5 (Figure 5B). Furthermore, PCM-0296174 reduced the infectious viral titer by 2 logs in a plaque assay (Figure S7). Finally, PCM-0296174 did not inhibit spike-mediated receptor interactions (Figure S8). Taken together, these experiments suggest that PCM-0296174 is a cell-permeable, selective S glycoprotein inhibitor that acts downstream of receptor binding.

DISCUSSION

To identify potential CoVs fusion inhibitors, we developed an HTS platform that relies on a phenotypic assay of infection using well-characterized, replication-deficient VSVΔG pseudoviruses that can be studied at biosafety level 2 (BSL-2) and express a fluorescent reporter upon infection. This allowed us to produce and accurately titer pseudoviruses featuring the S glycoproteins from SARS-CoV-2 variants and MERS-CoV, which was essential for establishing pseudoviruses preparation with titers of 10^4 infections per mL (Figure 1F). If the titers had dropped below 10^3 infections per mL, the feasibility of using 384-well plates would have been compromised, rendering the screening process both economically and logistically prohibitive.

We chose a fast-replicating VSV-based system encoding a fluorescent reporter, instead of the commonly used luciferase. The advantages of using a fluorescent reporter include direct measurement of single infection events as opposed to averaging across the whole population, high signal-to-noise ratio, and reduced sample processing.[49] The advantage of using a fast-replicating system is that infection can be quantified after 24 h post-infection.[43,44] Moreover, fluorescent reporters with different wavelengths enable the simultaneous examination of multiple viruses under the same experimental conditions (Figure 1G). The disadvantage of using VSV is that not all glycoproteins can be pseudotyped efficiently.

We leveraged the HTS platform to screen a comprehensive library of approximately 200,000 compounds, targeting potential CoV fusion inhibitors (Figure 3A). Our three-tiered assay incorporated two class I viral glycoproteins from phylogenetically distant CoVs (SARS-CoV-2 and MERS-CoV) and a class III glycoprotein from VSV[61,62] (Figure 3A). The primary screen against VSVΔG-S$_W$ yielded 733 compounds with inhibitory activity, including known inhibitors of proteases, ubiquitin-specific peptidases, and viral gene expression regulated by the HSP90 protein family. The secondary screen showed that most of these compounds also inhibit VSVΔG-G, yielding only 65 putative spike-specific inhibitors. Finally, the tertiary screen against VSVΔG-S$_M$ is effective in identifying compounds that inhibit the entry of CoV-S pseudoviruses downstream of receptor binding. Thus, the tertiary screen highlighted four compounds and the known TMPRSS2 inhibitor Nafamostat (Figures 3C and 3D). Our three-tier assay, while effective in identifying compounds that specifically inhibit the entry of pseudoviruses bearing the SARS-CoV-2 and MERS-CoV spike proteins, is unable to definitively distinguish between compounds that directly target the spike protein and those that act on host cellular proteins involved in the S2-mediated fusion process.

Following validation, only PCM-0163855 was retained as an inhibitor of S glycoprotein-mediated entry, acting downstream of receptor binding (Figure 4) and its sulfoxide derivative PCM-0282478 inhibited VSVΔG-S$_W$, VSVΔG-S$_o$, VSVΔG-S$_M$, and *bona fide* SARS-CoV-2 Delta virus replication (Figure 5). Finally, we showed that only one of the PCM-0282478 derived enantiomers, PCM-0296174, inhibits VSVΔG-S$_W$, VSVΔG-S$_o$, VSVΔG-S$_M$, and *bona fide* SARS-CoV-2 Delta virus replication, demonstrating its potential as a broad-spectrum inhibitor of CoVs. Note that we observed the Omicron CH.1.1 variant yielded an IC_{50} value with higher variability and no inhibitory activity against the XBB.1.5 variant (Figure 5). This may suggest that the unique mutations in the XBB.1.5 variant may alter the binding site for PCM-0296174 on the spike protein. Furthermore, given the likely poor solubility of PCM-0296174 (indicated by a calculated log D of 4), it is possible that we are underestimating the calculated IC_{50} values for variants that are well inhibited and cannot calculate it for the CH.1.1 variant. Synthesizing more soluble and active derivatives of PCM-0296174 will likely help clarify the breadth of selectivity and mode of action. Intriguingly, Nafamostat failed to inhibit *bona fide* SARS-CoV-2 Delta virus replication, perhaps due to the capacity of CoVs to infect cells in a TMPRSS2-independent pathway[63,64] (Figure S4).

Our findings reinforce the utility of the HTS platform in identifying CoVs inhibitors with the potential to deepen our understanding of coronavirus biology. It also highlights the significance of rigorous compound triage, which is instrumental in averting the dissemination of

ambiguous results. The discovery of PCM-0296174, a previously unreported compound that we synthesized and separated from the racemic mixture, as a promising compound with broad-spectrum antiviral will surely catalyze future research. Hence, the present study lays the groundwork for potential development of small molecules, holding promise for mitigating the impacts of future pandemics.

Limitations of the study

We provide a proof-of-concept demonstration that VSVΔG pseudotypes that express a fluorescent reporter can be used for robust high-throughput phenotypic screening targeting viral entry. While we speculate that the identified compounds target the conserved S2-domain of the CoV spike protein, our study does not provide direct evidence showing specific binding or the mode of action.

While PCM-0282478 and its active enantiomer exhibited promising broad-spectrum inhibitory activity against SARS-CoV-2 variants and MERS-CoV in pseudovirus- and *bona fide* virus-based assays, the efficacy of these compounds *in vivo* remains to be determined. In conclusion, our work provides a starting point for identifying potential antivirals.

STAR★METHODS

Detailed methods are provided in the online version of this paper and include the following:

- KEY RESOURCES TABLE
- RESOURCE AVAILABILITY
  - Lead contact
  - Materials availability
  - Data and code availability
- EXPERIMENTAL MODEL AND STUDY PARTICIPANT DETAILS
  - Cell lines
  - SARS-CoV-2 virus
- METHOD DETAILS
  - DNA constructs
  - Preparation of VSVΔG pseudoviruses
  - Viral titer
  - Compound libraries
  - Phenotypic assay: pseudotype-based HTS imaging inhibition assay
  - Dose response assay
  - Cell viability assay
  - Spike-ACE2 binding assay
  - Liquid chromatography-mass spectrometry (LC/MS)
  - Synthesis of PCM-0163855 and PCM-0282478
  - SARS-CoV-2 replication assay
  - SARS-CoV-2 plaque assay
- QUANTIFICATION AND STATISTICAL ANALYSIS
  - Statistical analysis and tools

SUPPLEMENTAL INFORMATION

Supplemental information can be found online at https://doi.org/10.1016/j.isci.2024.110019.

AUTHOR CONTRIBUTIONS

O.A., S.K., and E.O.P. conceived the study, designed, and executed the experiments with contributions from Y.E.A. and N.S.; S.K., N.K., H.M.B., and O.A. performed and analyzed the screen. K.S. performed the mass spectroscopy experiments, compound purification, and

synthesis. J.C. and F.A. supervised all experiments performed under BSL-3 conditions, and J.C., E.G., and J.T.-R. performed experiments with SARS-CoV-2 viruses. S.K. and O.A. wrote the manuscript with inputs from all authors.

DECLARATION OF INTERESTS

A patent application based on the findings of this paper has been filed.

REFERENCES

1. Hartenian, E., Nandakumar, D., Lari, A., Ly, M., Tucker, J.M., and Glaunsinger, B.A. (2020). The molecular virology of coronaviruses. J. Biol. Chem. 295, 12910–12934. https://doi.org/10.1074/jbc.rev120.013930.

2. Belouzard, S., Millet, J.K., Licitra, B.N., and Whittaker, G.R. (2012). Mechanisms of Coronavirus Cell Entry Mediated by the Viral Spike Protein. Viruses 4, 1011–1033. https://doi.org/10.3390/v4061011.

3. Walls, A.C., Tortorici, M.A., Snijder, J., Xiong, X., Bosch, B.-J., Rey, F.A., and Veesler, D. (2017). Tectonic conformational changes of a coronavirus spike glycoprotein promote membrane fusion. Proc. Natl. Acad. Sci. USA 114, 11157–11162. https://doi.org/10.1073/pnas.1708727114.

4. Jackson, C.B., Farzan, M., Chen, B., and Choe, H. (2022). Mechanisms of SARS-CoV-2 entry into cells. Nat. Rev. Mol. Cell Biol. 23, 3–20. https://doi.org/10.1038/s41580-021-00418-x.

5. Melo-Filho, C.C., Bobrowski, T., Martin, H.-J., Sessions, Z., Popov, K.I., Moorman, N.J., Baric, R.S., Muratov, E.N., and Tropsha, A. (2022). Conserved coronavirus proteins as targets of broad-spectrum antivirals. Antivir. Res. 204, 105360. https://doi.org/10.1016/j.antiviral.2022.105360.

6. Liu, D.X., Fung, T.S., Chong, K.K.-L., Shukla, A., and Hilgenfeld, R. (2014). Accessory proteins of SARS-CoV and other coronaviruses. Antivir. Res. 109, 97–109. https://doi.org/10.1016/j.antiviral.2014.06.013.

7. Walls, A.C., Park, Y.-J., Tortorici, M.A., Wall, A., McGuire, A.T., and Veesler, D. (2020). Structure, Function, and Antigenicity of the SARS-CoV-2 Spike Glycoprotein. Cell 181, 281–292.e6. https://doi.org/10.1016/j.cell.2020.02.058.

8. Patel, R., Kaki, M., Potluri, V.S., Kahar, P., and Khanna, D. (2022). A comprehensive review of SARS-CoV-2 vaccines: Pfizer, Moderna & Johnson & Johnson. Hum. Vaccines Immunother. 18, 2002083. https://doi.org/10.1080/21645515.2021.2002083.

9. Harvey, W.T., Carabelli, A.M., Jackson, B., Gupta, R.K., Thomson, E.C., Harrison, E.M., Ludden, C., Reeve, R., Rambaut, A., COVID-19 Genomics UK COG-UK Consortium, et al. (2021). SARS-CoV-2 variants, spike mutations and immune escape. Nat. Rev. Microbiol. 19, 409–424. https://doi.org/10.1038/s41579-021-00573-0.

10. Dejnirattisai, W., Huo, J., Zhou, D., Zahradník, J., Supasa, P., Liu, C., Duyvesteyn, H.M.E., Ginn, H.M., Mentzer, A.J., Tuekprakhon, A., et al. (2022). SARS-CoV-2 Omicron-B.1.1.529 leads to widespread escape from neutralizing antibody responses. Cell 185, 467–484.e15. https://doi.org/10.1016/j.cell.2021.12.046.

11. Willett, B.J., Grove, J., MacLean, O.A., Wilkie, C., De Lorenzo, G., Furnon, W., Cantoni, D., Scott, S., Logan, N., Ashraf, S., et al. (2022). SARS-CoV-2 Omicron is an immune escape variant with an altered cell entry pathway. Nat. Microbiol. 7, 1161–1179. https://doi.org/10.1038/s41564-022-01143-7.

12. Carabelli, A.M., Peacock, T.P., Thorne, L.G., Harvey, W.T., Hughes, J., COVID-19 Genomics UK Consortium, Peacock, S.J., Barclay, W.S., de Silva, T.I., Towers, G.J., and Robertson, D.L. (2023). SARS-CoV-2 variant biology: immune escape, transmission and fitness. Nat. Rev. Microbiol. 21, 162–177. https://doi.org/10.1038/s41579-022-00841-7.

13. Li, F., Li, W., Farzan, M., and Harrison, S.C. (2005). Structure of SARS Coronavirus Spike Receptor-Binding Domain Complexed with Receptor. Science 309, 1864–1868. https://doi.org/10.1126/science.1116480.

14. Lan, J., Ge, J., Yu, J., Shan, S., Zhou, H., Fan, S., Zhang, Q., Shi, X., Wang, Q., Zhang, L., and Wang, X. (2020). Structure of the SARS-CoV-2 spike receptor-binding domain bound to the ACE2 receptor. Nature 581, 215–220. https://doi.org/10.1038/s41586-020-2180-5.

15. Lu, G., Hu, Y., Wang, Q., Qi, J., Gao, F., Li, Y., Zhang, Y., Zhang, W., Yuan, Y., Bao, J., et al. (2013). Molecular basis of binding between novel human coronavirus MERS-CoV and its receptor CD26. Nature 500, 227–231. https://doi.org/10.1038/nature12328.

16. Baggen, J., Jacquemyn, M., Persoons, L., Vanstreels, E., Pye, V.E., Wrobel, A.G., Calvaresi, V., Martin, S.R., Roustan, C., Cronin, N.B., et al. (2023). TMEM106B is a receptor mediating ACE2-independent SARS-CoV-2 cell entry. Cell 186, 3427–3442.e22. https://doi.org/10.1016/j.cell.2023.06.005.

17. Glowacka, I., Bertram, S., Müller, M.A., Allen, P., Soilleux, E., Pfefferle, S., Steffen, I., Tsegaye, T.S., He, Y., Gnirss, K., et al. (2011). Evidence that TMPRSS2 Activates the Severe Acute Respiratory Syndrome Coronavirus Spike Protein for Membrane Fusion and Reduces Viral Control by the Humoral Immune Response. J. Virol. 85, 4122–4134. https://doi.org/10.1128/jvi.02232-10.

18. Shirato, K., Kawase, M., and Matsuyama, S. (2013). Middle East Respiratory Syndrome Coronavirus Infection Mediated by the Transmembrane Serine Protease TMPRSS2. J. Virol. 87, 12552–12561. https://doi.org/10.1128/jvi.01890-13.

19. Hoffmann, M., Kleine-Weber, H., Schroeder, S., Krüger, N., Herrler, T., Erichsen, S., Schiergens, T.S., Herrler, G., Wu, N.-H., Nitsche, A., et al. (2020). SARS-CoV-2 Cell Entry Depends on ACE2 and TMPRSS2 and Is Blocked by a Clinically Proven Protease Inhibitor. Cell 181, 271–280.e8. https://doi.org/10.1016/j.cell.2020.02.052.

20. Bosch, B.J., Bartelink, W., and Rottier, P.J.M. (2008). Cathepsin L Functionally Cleaves the Severe Acute Respiratory Syndrome Coronavirus Class I Fusion Protein Upstream of Rather than Adjacent to the Fusion Peptide. J. Virol. 82, 8887–8890. https://doi.org/10.1128/jvi.00415-08.

21. Zhao, M.-M., Yang, W.-L., Yang, F.-Y., Zhang, L., Huang, W.-J., Hou, W., Fan, C.-F., Jin, R.-H., Feng, Y.-M., Wang, Y.-C., and Yang, J.K. (2021). Cathepsin L plays a key role in SARS-CoV-2 infection in humans and humanized mice and is a promising target for new drug development. Signal Transduct. Targeted Ther. 6, 134. https://doi.org/10.1038/s41392-021-00558-8.

22. Hoffmann, M., Schroeder, S., Kleine-Weber, H., Müller, M.A., Drosten, C., and Pöhlmann, S. (2020). Nafamostat Mesylate Blocks Activation of SARS-CoV-2: New Treatment Option for COVID-19. Antimicrob Agents Ch 64, e00754-20. https://doi.org/10.1128/aac.00754-20.

23. Tang, M., Zhang, X., Huang, Y., Cheng, W., Qu, J., Gui, S., Li, L., and Li, S. (2022). Peptide-based inhibitors hold great promise as the broad-spectrum agents against coronavirus. Front. Microbiol. 13, 1093646. https://doi.org/10.3389/fmicb.2022.1093646.

24. Shapira, T., Monreal, I.A., Dion, S.P., Buchholz, D.W., Imbiakha, B., Olmstead, A.D., Jager, M., Désilets, A., Gao, G., Martins, M., et al. (2022). A TMPRSS2 inhibitor acts as a pan-SARS-CoV-2 prophylactic and therapeutic. Nature 605, 340–348. https://doi.org/10.1038/s41586-022-04661-w.

25. Zang, R., Gomez Castro, M.F., McCune, B.T., Zeng, Q., Rothlauf, P.W., Sonnek, N.M., Liu, Z., Brulois, K.F., Wang, X., Greenberg, H.B., et al. (2020). TMPRSS2 and TMPRSS4 promote SARS-CoV-2 infection of human small intestinal enterocytes. Sci. Immunol. 5, eabc3582. https://doi.org/10.1126/sciimmunol.abc3582.

26. Wu, Y., and Zhao, S. (2020). Furin cleavage sites naturally occur in coronaviruses. Stem Cell Res. 50, 102115. https://doi.org/10.1016/j.scr.2020.102115.

27. Garry, R.F. (2022). SARS-CoV-2 furin cleavage site was not engineered. Proc. Natl. Acad. Sci. USA 119, e2211107119. https://doi.org/10.1073/pnas.2211107119.

28. Ng, K.W., Faulkner, N., Cornish, G.H., Rosa, A., Harvey, R., Hussain, S., Ulferts, R., Earl, C., Wrobel, A.G., Benton, D.J., et al. (2020).

Preexisting and de novo humoral immunity to SARS-CoV-2 in humans. Science 370, 1339–1343. https://doi.org/10.1126/science.abe1107.

29. Jaago, M., Rähni, A., Pupina, N., Pihlak, A., Sadam, H., Tuvikene, J., Avarlaid, A., Planken, A., Planken, M., Haring, L., et al. (2022). Differential patterns of cross-reactive antibody response against SARS-CoV-2 spike protein detected for chronically ill and healthy COVID-19 naïve individuals. Sci. Rep. 12, 16817. https://doi.org/10.1038/s41598-022-20849-6.

30. Podbilewicz, B. (2014). Virus and Cell Fusion Mechanisms. Annu. Rev. Cell Dev. Biol. 30, 111–139. https://doi.org/10.1146/annurev-cellbio-101512-122422.

31. Cui, J., Li, F., and Shi, Z.-L. (2019). Origin and evolution of pathogenic coronaviruses. Nat. Rev. Microbiol. 17, 181–192. https://doi.org/10.1038/s41579-018-0118-9.

32. Jaimes, J.A., André, N.M., Chappie, J.S., Millet, J.K., and Whittaker, G.R. (2020). Phylogenetic Analysis and Structural Modeling of SARS-CoV-2 Spike Protein Reveals an Evolutionary Distinct and Proteolytically Sensitive Activation Loop. J. Mol. Biol. 432, 3309–3325. https://doi.org/10.1016/j.jmb.2020.04.009.

33. Trigueiro-Louro, J., Correia, V., Figueiredo-Nunes, I., Gíria, M., and Rebelo-de-Andrade, H. (2020). Unlocking COVID therapeutic targets: A structure-based rationale against SARS-CoV-2, SARS-CoV and MERS-CoV Spike. Comput. Struct. Biotechnol. J. 18, 2117–2131. https://doi.org/10.1016/j.csbj.2020.07.017.

34. Beigel, J.H., Tomashek, K.M., Dodd, L.E., Mehta, A.K., Zingman, B.S., Kalil, A.C., Hohmann, E., Chu, H.Y., Luetkemeyer, A., Kline, S., et al. (2020). Remdesivir for the Treatment of Covid-19 — Final Report. N. Engl. J. Med. 383, 1813–1826. https://doi.org/10.1056/nejmoa2007764.

35. Bernal, A.J., Silva, M.M.G. da, Musungaie, D.B., Kovalchuk, E., Gonzalez, A., Reyes, V.D., Martín-Quirós, A., Caraco, Y., Williams-Diaz, A., Brown, M.L., et al. (2021). Molnupiravir for Oral Treatment of Covid-19 in Nonhospitalized Patients. N. Engl. J. Med. 386, 509–520. https://doi.org/10.1056/nejmoa2116044.

36. Tian, F., Chen, Z., and Feng, Q. (2023). Nirmatrelvir–ritonavir compared with other antiviral drugs for the treatment of COVID-19 patients: A systematic review and meta-analysis. J. Med. Virol. 95, e28732. https://doi.org/10.1002/jmv.28732.

37. Madrid, P.B., Chopra, S., Manger, I.D., Gilfillan, L., Keepers, T.R., Shurtleff, A.C., Green, C.E., Iyer, L.V., Dilks, H.H., Davey, R.A., et al. (2013). A Systematic Screen of FDA-Approved Drugs for Inhibitors of Biological Threat Agents. PLoS One 8, e60579. https://doi.org/10.1371/journal.pone.0060579.

38. Ellinger, B., Pohlmann, D., Woens, J., Jäkel, F.M., Reinshagen, J., Stocking, C., Prassolov, V.S., Fehse, B., and Riecken, K. (2020). A High-Throughput HIV-1 Drug Screening Platform, Based on Lentiviral Vectors and Compatible with Biosafety Level-1. Viruses 12, 580. https://doi.org/10.3390/v12050580.

39. Xu, M., Lee, E.M., Wen, Z., Cheng, Y., Huang, W.-K., Qian, X., TCW, J., Kouznetsova, J., Ogden, S.C., Hammack, C., et al. (2016). Identification of small-molecule inhibitors of Zika virus infection and induced neural cell

death via a drug repurposing screen. Nat. Med. 22, 1101–1107. https://doi.org/10.1038/nm.4184.

40. Zhou, Y., Hou, Y., Shen, J., Huang, Y., Martin, W., and Cheng, F. (2020). Network-based drug repurposing for novel coronavirus 2019-nCoV/SARS-CoV-2. Cell Discov. 6, 14. https://doi.org/10.1038/s41421-020-0153-3.

41. Gordon, D.E., Jang, G.M., Bouhaddou, M., Xu, J., Obernier, K., White, K.M., O'Meara, M.J., Rezelj, V.V., Guo, J.Z., Swaney, D.L., et al. (2020). A SARS-CoV-2 protein interaction map reveals targets for drug repurposing. Nature 583, 459–468. https://doi.org/10.1038/s41586-020-2286-9.

42. Riva, L., Yuan, S., Yin, X., Martin-Sancho, L., Matsunaga, N., Pache, L., Burgstaller-Muehlbacher, S., De Jesus, P.D., Teriete, P., Hull, M.V., et al. (2020). Discovery of SARS-CoV-2 antiviral drugs through large-scale compound repurposing. Nature 586, 113–119. https://doi.org/10.1038/s41586-020-2577-1.

43. Xu, M., Pradhan, M., Gorshkov, K., Petersen, J.D., Shen, M., Guo, H., Zhu, W., Klumpp-Thomas, C., Michael, S., Itkin, M., et al. (2022). A high throughput screening assay for inhibitors of SARS-CoV-2 pseudotyped particle entry. SLAS Discov. 27, 86–94. https://doi.org/10.1016/j.slasd.2021.12.005.

44. Mediouni, S., Mou, H., Otsuka, Y., Jablonski, J.A., Adcock, R.S., Batra, L., Chung, D.-H., Rood, C., de Vera, I.M.S., Rahaim, R., Jr., et al. (2022). Identification of potent small molecule inhibitors of SARS-CoV-2 entry. SLAS Discov. 27, 8–19. https://doi.org/10.1016/j.slasd.2021.10.012.

45. Zhang, Z.-R., Zhang, Y.-N., Li, X.-D., Zhang, H.-Q., Xiao, S.-Q., Deng, F., Yuan, Z.-M., Ye, H.-Q., and Zhang, B. (2020). A cell-based large-scale screening of natural compounds for inhibitors of SARS-CoV-2. Signal Transduct. Targeted Ther. 5, 218. https://doi.org/10.1038/s41392-020-00343-z.

46. Boby, M.L., Fearon, D., Ferla, M., Filep, M., Koekemoer, L., Robinson, M.C., Consortium, T.C.M., Chodera, J.D., Lee, A.A., London, N., et al. (2023). Open science discovery of potent noncovalent SARS-CoV-2 main protease inhibitors. Science 382, eabo7201. https://doi.org/10.1126/science.abo7201.

47. Ton, A.-T., Pandey, M., Smith, J.R., Ban, F., Fernandez, M., and Cherkasov, A. (2022). Targeting SARS-CoV-2 papain-like protease in the postvaccine era. Trends Pharmacol. Sci. 43, 906–919. https://doi.org/10.1016/j.tips.2022.08.008.

48. Luttens, A., Gullberg, H., Abdurakhmanov, E., Vo, D.D., Akaberi, D., Talibov, V.O., Nekhotiaeva, N., Vangeel, L., De Jonghe, S., Jochmans, D., et al. (2022). Ultralarge Virtual Screening Identifies SARS-CoV-2 Main Protease Inhibitors with Broad-Spectrum Activity against Coronaviruses. J. Am. Chem. Soc. 144, 2905–2920. https://doi.org/10.1021/jacs.1c08402.

49. Yang, L., Pei, R.J., Li, H., Ma, X.N., Zhou, Y., Zhu, F.H., He, P.L., Tang, W., Zhang, Y.C., Xiong, J., et al. (2021). Identification of SARS-CoV-2 entry inhibitors among already approved drugs. Acta Pharmacol. Sin. 42, 1347–1353. https://doi.org/10.1038/s41401-020-00556-6.

50. Shen, L., Niu, J., Wang, C., Huang, B., Wang, W., Zhu, N., Deng, Y., Wang, H., Ye, F., Cen, S., and Tan, W. (2019). High-Throughput Screening and Identification of Potent Broad-Spectrum Inhibitors of Coronaviruses. J. Virol.

93, e00023-19. https://doi.org/10.1128/jvi.00023-19.

51. Haid, S., Matthaei, A., Winkler, M., Sake, S.M., Gunesch, A.P., Milke, V., Köhler, N.M., Rückert, J., Vieyres, G., Kühl, D., et al. (2024). Repurposing screen identifies novel candidates for broad-spectrum coronavirus antivirals and druggable host targets. Antimicrob. Agents Chemother. 68, e01210-23. https://doi.org/10.1128/aac.01210-23.

52. Whitt, M.A. (2010). Generation of VSV pseudotypes using recombinant ΔG-VSV for studies on virus entry, identification of entry inhibitors, and immune responses to vaccines. J. Virol. Methods 169, 365–374. https://doi.org/10.1016/j.jviromet.2010.08.006.

53. Sapir, A., Avinoam, O., Podbilewicz, B., and Chernomordik, L.V. (2008). Viral and Developmental Cell Fusion Mechanisms: Conservation and Divergence. Dev. Cell 14, 11–21. https://doi.org/10.1016/j.devcel.2007.12.008.

54. Vance, T.D.R., and Lee, J.E. (2020). Virus and eukaryote fusogen superfamilies. Curr. Biol. 30, R750–R754. https://doi.org/10.1016/j.cub.2020.05.029.

55. White, J.M., Delos, S.E., Brecher, M., and Schornberg, K. (2008). Structures and Mechanisms of Viral Membrane Fusion Proteins: Multiple Variations on a Common Theme. Crit Rev Biochem Mol 43, 189–219. https://doi.org/10.1080/10409230802058320.

56. Smale, S.T. (2010). Luciferase Assay. Cold Spring Harb. Protoc. 2010, pdb.prot5421. https://doi.org/10.1101/pdb.prot5421.

57. Howard, M.W., Travanty, E.A., Jeffers, S.A., Smith, M.K., Wennier, S.T., Thackray, L.B., and Holmes, K.V. (2008). Aromatic Amino Acids in the Juxtamembrane Domain of Severe Acute Respiratory Syndrome Coronavirus Spike Glycoprotein Are Important for Receptor-Dependent Virus Entry and Cell-Cell Fusion. J. Virol. 82, 2883–2894. https://doi.org/10.1128/jvi.01805-07.

58. Tien, C.-F., Tsai, W.-T., Chen, C.H., Chou, H.-J., Zhang, M.M., Lin, J.-J., Lin, E.-J., Dai, S.-S., Ping, Y.-H., Yu, C.-Y., et al. (2022). Glycosylation and S-palmitoylation regulate SARS-CoV-2 spike protein intracellular trafficking. iScience 25, 104709. https://doi.org/10.1016/j.isci.2022.104709.

59. Condor Capcha, J.M., Lambert, G., Dykxhoorn, D.M., Salerno, A.G., Hare, J.M., Whitt, M.A., Pahwa, S., Jayaweera, D.T., and Shehadeh, L.A. (2021). Generation of SARS-CoV-2 Spike Pseudotyped Virus for Viral Entry and Neutralization Assays: A 1-Week Protocol. Frontiers Cardiovasc Medicine 7, 618651. https://doi.org/10.3389/fcvm.2020.618651.

60. Zhang, J.-H., Chung, T.D.Y., and Oldenburg, K.R. (1999). A simple statistical parameter for use in evaluation and validation of high throughput screening assays. J. Biomol. Screen 4, 67–73. https://doi.org/10.1177/108705719900400206.

61. Kielian, M., and Rey, F.A. (2006). Virus membrane-fusion proteins: more than one way to make a hairpin. Nat. Rev. Microbiol. 4, 67–76. https://doi.org/10.1038/nrmicro1326.

62. Weissenhorn, W., Hinz, A., and Gaudin, Y. (2007). Virus membrane fusion. FEBS Lett. 581, 2150–2155. https://doi.org/10.1016/j.febslet.2007.01.093.

63. Koch, J., Uckeley, Z.M., Doldan, P., Stanifer, M., Boulant, S., and Lozach, P.Y. (2021).

TMPRSS2 expression dictates the entry route used by SARS-CoV-2 to infect host cells. EMBO J. *40*, e107821. https://doi.org/10.15252/embj.2021107821.

64. Wang, H., Yang, Q., Liu, X., Xu, Z., Shao, M., Li, D., Duan, Y., Tang, J., Yu, X., Zhang, Y., et al. (2023). Structure-based discovery of dual pathway inhibitors for SARS-CoV-2 entry. Nat. Commun. *14*, 7574. https://doi.org/10.1038/s41467-023-42527-5.

65. Strobelt, R., Adler, J., Paran, N., Yahalom-Ronen, Y., Melamed, S., Politi, B., Shulman, Z., Schmiedel, D., and Shaul, Y. (2022). Imatinib inhibits SARS-CoV-2 infection by an off-target-mechanism. Sci. Rep. *12*, 5758. https://doi.org/10.1038/s41598-022-09664-1.

66. Avinoam, O., Fridman, K., Valansi, C., Abutbul, I., Zeev-Ben-Mordehai, T., Maurer, U.E., Sapir, A., Danino, D., Grünewald, K., White, J.M., and Podbilewicz, B. (2011). Conserved Eukaryotic Fusogens Can Fuse Viral Envelopes to Cells. Science *332*, 589–592. https://doi.org/10.1126/science.1202333.

67. Shang, J., Ye, G., Shi, K., Wan, Y., Luo, C., Aihara, H., Geng, Q., Auerbach, A., and Li, F. (2020). Structural basis of receptor recognition by SARS-CoV-2. Nature *581*, 221–224. https://doi.org/10.1038/s41586-020-2179-y.

68. Stringer, C., Wang, T., Michaelos, M., and Pachitariu, M. (2021). Cellpose: a generalist algorithm for cellular segmentation. Nat.

Methods *18*, 100–106. https://doi.org/10.1038/s41592-020-01018-x.

69. Amanat, F., Stadlbauer, D., Strohmeier, S., Nguyen, T.H.O., Chromikova, V., McMahon, M., Jiang, K., Arunkumar, G.A., Jurczyszak, D., Polanco, J., et al. (2020). A serological assay to detect SARS-CoV-2 seroconversion in humans. Nat. Med. *26*, 1033–1036. https://doi.org/10.1038/s41591-020-0913-5.

70. Sujatha, K., and Khanapurmath, N. (2021). Solvatochromic Studies On 4-(1,4 diphenyl-1H imidazole-2-ylthio)-2H-chromen-2-one. Rasayan J. Chem. *14*, 2263–2272. https://doi.org/10.31788/rjc.2021.1446171.

STAR★METHODS

KEY RESOURCES TABLE

REAGENT or RESOURCE	SOURCE	IDENTIFIER
Antibodies		
anti-G neutralizing antibody	Absolute Antibody	Cat# Ab01402–2.0; RRID: AB_3099672
Bacterial and virus strains		
Human CD26/DPP4 pre-packaged lentiviral particles	G&P Biosciences	Cat# LTV-CD26
Delta B.1.617.2	Virus and Immunity Unit in Institut Pasteur (Paris, France)	NA
XBB.1.5	National Reference Centre for Respiratory Viruses hosted by Institut Pasteur (Paris, France)	hCoV-19/France/PDL-IPP58867/2022
CH.1.1	National Reference Centre for Respiratory Viruses hosted by Institut Pasteur (Paris, France)	hCoV-19/France/NAQ-IPP58166/2022
Chemicals, peptides, and recombinant proteins		
1-(4-chlorophenyl)-4-phenyl-1H-imidazole-2-thiol	This paper	NA
1,8-Diazabicyclo[5.4.0]undec-7-ene	Sigma Aldrich	Cat# 139009
Acetonitrile	Bio-Lab	Cat# 012035-2.5L
Acetonitrile (HPLC grade)	Merck	Cat# 1000302500
Agarose	Sigma Aldrich	Cat# 05066
Bioactive Screening Libraries	Selleck Chemicals	NA
Sodium chloride	Sigma Aldrich	Cat# S9888
Calcein	Life Technologies	Cat# C3099
Camptothecin	Sigma Aldrich	Cat# PHL89593
Crystal violet solution	Merck	Cat# HT901
Dichlormethane	Bio-lab	Cat# 13790601
Diisopropylethyl amine	Sigma Aldrich	Cat# D125806
Dimethylformamide	Sigma Aldrich	Cat# 227056
DIVERset-CL	Chembridge	NA
Diversity Library	ChemDiv	NA
Drug-Like Set	Enamine	NA
Ethyl acetate	Bio-lab	Cat# 5400521
Ethyl bromo acetate	Sigma Aldrich	Cat# 133973
Formic acid (HPLC grade)	Bio-lab	Cat# 069141
Hexafluorophosphate azabenzotriazole tetramethyl uronium	Sigma Aldrich	Cat# 445460
HitFinder Collection	Maybridge	NA
Hoechst 33342	Thermo Fisher Scientific	Cat# 62249
Hydrochloric acid	Bio-Lab	Cat# 0584601
Lithium hydroxide	Sigma Aldrich	Cat# 545856
meta-Chloroperoxybenzoic acid	Sigma Aldrich	Cat# 273031
Propidium Iodide	Life Technologies	Cat# P3566
Remdesivir	Selleck Chemicals	Cat# GS-5734
Sodium sulfate	Sigma Aldrich	Cat# 239313

Continued

REAGENT or RESOURCE	SOURCE	IDENTIFIER
Sodium sulfite	Sigma Aldrich	Cat# 239321
Soluble Spike	The Dana and Yossie Hollander Center for Structural Proteomics (Weizmann Institute of Science)	
Tetrahydrofuran	Sigma Aldrich	Cat# 186562
Trifluoroacetic acid	Sigma Aldrich	Cat# T6508
Water (HPLC grade)	Merck	Cat# 1153332500
Critical commercial assays		
CellTiter-Glo luminescent cell viability kit	Promega	Cat# G7570
Gibson Assembly HiFi master mix	Thermo Fisher Scientific	Cat# A46627
Luna Universal One-Step RT-qPCR Kit	New England Biolabs	Cat# E3005S
SARS-CoV-2 Spike S1 RBD: ACE2 Inhibitor Screening Assay Kit	BPS Bioscience	Cat# 79936
Experimental models: Cell lines		
BHK-21	ATCC	Cat# CCL-10
HEK-293T	ATCC	Cat# CRL-3216
HEK-293T-ACE2	Prof. Yosef Shaul (Weizmann Institute of Science)	https://doi.org/10.1038/s41598-022-09664-1
HEK-293T-ACE2-TMPRSS2	Prof. Yosef Shaul (Weizmann Institute of Science)	https://doi.org/10.1038/s41598-022-09664-1
HEK-293T-ACE2-TMPRSS2-DPP4	This paper	NA
Vero E6	ATCC	Cat# CRL-1586
Vero E6-TMPRSS2	NIBSC	Cat# 100978
Oligonucleotides		
V1:CGCACAAGGTCCACGTCCACGGCTCCACCGAGACATCCC V2:AGAAAAACTGAATGAATCATGCTAGCCAGCTTGGGTC	This paper	NA
I1: GGAGACCCAAGCTGGCTAGCATGATT CATTCAGTTTTTCTGCTCATGTTTC I2: TGGGATGTCTCGGTG GAGCCGTGG ACGTGGACCTTGTGC	This paper	NA
N gene region of SARS-CoV-2 5′-TAATCAGACAAGGAACTGATTA-3′ 5′-CGAAGGTGTGACTTCCATG-3′	This paper	NA
Recombinant DNA		
pCAGGS-G	Prof. Benjamin Podbilewicz (Technion - Israel Institute of Technology)	https://doi.org/10.1126/science.1202333
pCG1-SARS2-Spike-HA	Prof. Gideon Schreiber (Weizmann Institute of Science)	NA
pCMV3-SARS2-Spike-Flag	Prof. Gideon Schreiber (Weizmann Institute of Science)	NA
pCMV3-SARS2-SpikeΔ19	Prof. Yosef Shaul (Weizmann Institute of Science)	https://doi.org/10.1038/s41598-022-09664-1
pCMV3-SARS2-SpikeΔ19-Flag	Prof. Yosef Shaul (Weizmann Institute of Science)	https://doi.org/10.1038/s41598-022-09664-1
pcDNA3.1-SARS-CoV-2-Spike-C9	Addgene	Cat# 145032
pcDNA3.1-SARS-CoV-2-S$_\alpha$-C9	This paper	NA

Continued

REAGENT or RESOURCE	SOURCE	IDENTIFIER
pcDNA3.1-SARS-CoV-2-S$_\delta$-C9	This paper	NA
pcDNA3.1-SARS-CoV-2-S$_o$-C9	This paper	NA
pcDNA3.1-MERS-Spike-C9	This paper	NA
Software and algorithms		
CDD vault	Collaborative Drug Discovery	RRID: SCR_025149
Cellpose	https://doi.org/10.1038/s41592-020-01018-x	RRID: SCR_021716
D360 software	Certara	RRID: SCR_025159
Excel	Microsoft	RRID: SCR_016137
Genedata Screener	Genedata	RRID: SCR_022506
MetaXpress CME	Molecular Devices	RRID: SCR_016654
Prism	GraphPad	RRID: SCR_002798
ZEN blue software 3.1	Carl Zeiss	RRID: SCR_013672
Other		
100 mm dish	Greiner	Cat# 664160
6-well plate	Corning	Cat# 3516
384 well plate	Greiner	Cat# 781091
Blasticidin	InvivoGen	Cat# ant-bl-1
Dulbecco's modified eagle medium	Thermo Fisher Scientific	Cat# 41965039; Cat# 31966047
Dulbecco's Phosphate-Buffered Saline	Biological Industries	Cat# 02-020-1A
Fetal bovine serum	Thermo Fisher Scientific	Cat# 12657-029; Cat# 31966047
Geneticin	Thermo Fisher Scientific	Cat# 11558616
HEPES	Biological Industries	Cat# 03-025-1B
JetPrime transfection reagent	Polyplus	Cat# 101000015
Polybrene infection reagent	Sigma Aldrich	Cat# TR-1003-G
Penicillin-streptomycin	Biological Industries/Thermo Fisher Scientific	Cat# 03-031-1B/Cat# 15140148
Puromycin	Sigma Aldrich	Cat# P4512
Silica	Sigma Aldrich	Cat# 60737

RESOURCE AVAILABILITY

Lead contact

Further information and requests for resources and reagents should be directed to and will be fulfilled by the lead contact, Ori Avinoam (ori.avinoam@weizmann.ac.il).

Materials availability

The plasmids and cells generated in this study will be available upon request.

Data and code availability

Data reported in this paper will be shared by the lead contact upon request. This paper does not report original code. Any additional information required to reanalyze the data reported in this paper is available from the lead contact upon request.

EXPERIMENTAL MODEL AND STUDY PARTICIPANT DETAILS

Cell lines

Baby Hamster Kidney cells (BHK-21; ATCC, USA) were maintained in Dulbecco's modified eagle medium (DMEM; Thermo Fisher Scientific, USA) supplemented with 10% fetal bovine serum (FBS; Thermo Fisher Scientific), 1% penicillin-streptomycin (PS, Biological Industries) and 25mM HEPES (Biological Industries).

Human Embryonic Kidney-293T cells (HEK-293T; ATCC), HEK-293T overexpressing either ACE2 (HEK-293T-ACE2) or both ACE2 and TMPRSS2 (HEK-293T-ACE2-TMPRSS2), or ACE2, DPP4 and TMPRSS2 (HEK-293T-ACE2-TMPRSS2-DPP4) were cultured in DMEM supplemented with 8.1% FBS, 1% PS, 25mM HEPES. HEK-293T-ACE2, HEK-293T-ACE2-TMPRSS2, and HEK-293T-ACE2-DPP4-TMPRSS2 were maintained by supplementing the culture medium with 1 μg/ml Puromycin (Sigma-Aldrich, USA), and 1.5 μg/ml Blasticidin (InvivoGen, USA) respectively. All cell lines were cultured in a 5% CO2 incubator at 37°C. HEK-293T-ACE2 and HEK-293T-ACE2-TMPRSS2 were a kind gifts from Yosef Shaul (Weizmann Institute of Science).[65] HEK-293T-ACE2-TMPRSS2-DPP4 cells were established by lentiviral transduction. 0.3 x 10^6 HEK-293T-ACE2-TMPRSS2 cells were seeded in each well of a 6-well plate (Corning, USA) and cultured to 70-80% confluency. The growth medium was replaced with 1 ml of medium containing human CD26/DPP4 pre-packaged lentiviral particles (G&P Biosciences, USA) at a multiplicity of infection (MOI) of 5. To enhance transduction efficiency, 1:1000 of polybrene infection reagent (Sigma-Aldrich) was added to the medium. The cells were incubated with the lentivirus for 24h at 37°C with 5% CO2. After the transduction period, the viral supernatant was removed, and a fresh growth medium containing 1 μg/ml Puromycin was added to the cells to initiate the selection process.

Vero E6 (ATCC) and Vero E6-TMPRSS2 (NIBSC, UK) were maintained in DMEM supplemented with 10% FBS, 1% PS. Vero E6-TMPRSS2 were maintained by supplementing the culture medium with 1 mg/ml Geneticin (Thermo Fisher Scientific).

All the cell lines were tested for mycoplasma contamination.

SARS-CoV-2 virus

Delta B.1.617.2: The variant was supplied by Virus and Immunity Unit in Institut Pasteur headed by Olivier Schwartz. It was isolated from a nasopharyngeal swab of a hospitalized patient who had returned from India. The swab was provided and sequenced by the Laboratoire de Virologie of the Hopital Européen Georges Pompidou (Assistance Publique des Hôpitaux de Paris).

XBB.1.5: The strain hCoV-19/France/PDL-IPP58867/2022 was supplied by the National Reference Centre for Respiratory Viruses hosted by Institut Pasteur (Paris, France) and headed by Dr. Etienne Simon-Lorière. The human sample from which strain hCoV-19/France/PDL-IPP58867/2022 was isolated has been provided from the Centre Hospitalier de Laval.

CH.1.1: The strain hCoV-19/France/NAQ-IPP58166/2022 was also supplied by the National Reference Centre for Respiratory Viruses hosted by Institut Pasteur (Paris, France). The human sample from which strain hCoV-19/France/NAQ-IPP58166/2022 was isolated has been provided from the Selas Cerballiance Charentes.

METHOD DETAILS

DNA constructs

pCAGGS-G, encoding the Vesicular Stomatitis Virus G glycoprotein from the Indiana serotype (VSV-G), was a kind gift from Benjamin Podbilewicz (Technion - Israel Institute of Technology).[66] pcDNA3.1-SARS-CoV-2-Spike-C9, encoding the Spike glycoprotein of Wuhan SARS-CoV-2 fused to a C-terminal C9 tag (S_W) was a kind gift from Fang Li (Addgene plasmid # 145032; http://n2t.net/addgene:145032; RRID:Addgene_145032).[67] pCG1-SARS2-Spike-HA, encoding the Wuhan SARS-CoV-2 Spike protein fused to a C-terminal HA tag was a kind gift from Gideon Schreiber, pCMV3-SARS2-Spike-Flag, encoding the Wuhan SARS-CoV-2 Spike protein fused to a C-terminal FLAG tag, pCMV3-SARS2-SpikeΔ19, encoding the Wuhan SARS-CoV-2 Spike protein with 19 amino acids removed at the cytoplasmic tail, and pCMV3-SARS2-SpikeΔ19-Flag, with an added C-terminal FLAG tag were a kind gift from and Yosef Shaul (Weizmann Institute of Science).[65] pcDNA3.1-SARS-CoV-2-$S_α$-C9, pcDNA3.1-SARS-CoV-2-$S_δ$-C9, and pcDNA3.1-SARS-CoV-2-S_o-C9 encoding the Spike glycoprotein of Wuhan SARS-CoV-2 variants fused to a C-terminal C9 tag were generated by DNA synthesis (GeneScript, USA). pcDNA3.1-MERS-Spike-C9, encoding the Spike glycoprotein of the MERS-CoV (S_M) fused to a C-terminal C9 tag was generated by sub-cloning the MERS Spike protein from a pLVX-EF1alpha-MERS-Spike plasmid (Weizmann Plasmid Bank) into a pcDNA3.1 expression plasmid using the GeneArt Gibson Assembly HiFi master mix (Thermo Fisher Scientific). The following primers were used to generate the vector fragment: Primers V1: CGCACAAGGTCCACGTCCACGGCTCCACCGAGACATCCC and V2: AGAAAAAC TGAATGAATCATGCTAGCCAGCTTGGGTC; template DNA: pcDNA3.1-SARS-Spike alpha and the insert fragment: Primers I1: GGAGACC CAAGCTGGC TAGCATGATTCATTCAGTTTTTCTGCTCATGTTTC and I2: TGGGATGTCTCGGTG GAGCCGTGGACGTGGACCTTGTGC; template DNA: pLVX-EF1alpha-MERS-Spike. The sequences of all the CoV Spikes are listed in the Table S4.

Preparation of VSVΔG pseudoviruses

To generate 5 ml of glycoprotein X complemented pseudoviruses (VSVΔG-X), 1.2×10^6 BHK-21 cells were plated in a 100 mm dish (Greiner, Austria) one day prior to transfection. The cells were transfected using JetPrime transfection reagent (Polyplus, France) at 75-80% confluence with 5 μg of a plasmid expressing the viral glycoprotein. 24 h post-transfection, cells were infected with VSVΔG-G pseudovirus at a MOI of 5, with 1:1000 of polybrene infection reagent. Cells were incubated for 1 h at 37°C in a 5% CO_2 incubator, and shaken every 15 min. Post infection, cells were washed six times with Dulbecco's Phosphate-Buffered Saline (DPBS, Biological Industries), and the medium was replaced with a 5 ml growth medium. 30 h post-infection, cells and the supernatant containing the pseudoviruses were collected and centrifuged at 500 g for 10 mins at 4°C. Pseudovirus suspension was collected, aliquoted, and frozen at -80°C for further experiments.

Viral titer

To accurately determine viral titers of VSVΔG complemented pseudoviruses at the conditions of the high throughput screen, 10 μl of pseudovirus suspension was dispensed in a 384-well plate (Greiner) in sextuplicate. Then, 10^3 HEK-293T-ACE2-TMPRSS2 cells were added to each

well and allowed to settle for 15 mins at RT before centrifugation at 1000g for 1 h at RT to maximize infection. The plates were subsequently incubated for 24 h in a 5% CO_2 incubator at 37°C.

After 24 hours, the plates were imaged using Cell Discoverer 7 (Carl Zeiss, Germany) in widefield mode with a sCMOS 702 camera (Carl Zeiss). Images were acquired using a Plan-APOCHROMAT 5x / 0.35 Autocorr Objective (Carl Zeiss). ZEN blue software 3.1 (Carl Zeiss) was used for image acquisition using 470 nm excitation for the acquisition of the infected channel. The infected cells were segmented and counted using Cellpose.[68] Infectious units/ml were extrapolated by calculating the geometric mean of the number of infected cells multiplied by 100 to convert the units from µl to ml. Where applicable, the pseudovirus containing supernatant was first incubated with anti-G neutralizing antibody (α-G; Absolute Antibody, UK) at a 1:1000 dilution for 1 h at room temperature (RT) to remove residual VSVΔG-G background infections before tittering.

Compound libraries

The compound collection of the Nancy and Stephen Grand Israel National Center for Personalized Medicine (G-INCPM) was used for screening (https://g-incpm.weizmann.ac.il/units/WohlDrugDiscovery/chemical-libraries). 173,227 unique compounds from commercial sub-collections were used. The composition of the screening set was 0.7% Bioactive Screening Libraries (Selleck Chemicals, USA), 7.6% HitFinder Collection (Maybridge, USA), 10.8% Drug-Like Set (Enamine, Ukraine), 26.8% DIVERset-CL (Chembridge, USA), 54.1% Diversity Library (ChemDiv, USA). Compounds were stored in 100% DMSO in acoustic dispenser certified plates. Hit compounds were purchased from Sigma-Aldrich, Aldrich Market Select (Sigma-Aldrich), Enamine or MolPort (Latvia) chemical suppliers.

Phenotypic assay: pseudotype-based HTS imaging inhibition assay

Compounds were spotted using Echo 555 Liquid Handler (Beckman Coulter, USA) on 384-well assay plates in 10 µM final concentration. To avoid background from any residual VSVΔG-G activity, pseudoviruses were incubated with α-G neutralizing antibody (1:5000) for 1 h at RT. Subsequently, 10 µl of the pseudovirus suspension were dispensed using Multidrop Combi (Thermo Fisher Scientific) and incubated with compounds for 15 mins at RT. HEK-293T-ACE2-TMPRSS2 were trypsinized, counted and diluted to 0.5×10^6 cells/ml. 20 µl of this cell suspension was dispensed (Multidrop Combi) in each well containing the compound and the neutralized pseudoviruses and incubated for an additional 15 mins at RT. To maximize infection, assay plates were then subjected to 1000g centrifugation for 1 h at RT and incubated overnight in a 5% CO_2 incubator at 37°C.

To account for the toxicity at 10 µM for a compound, wells were stained for nuclei with 5 µg/ml Hoechst 33342 (Thermo Fisher Scientific) and incubated for 10 mins at 37°C, 5% CO_2 before live cell imaging was done by ImageXpressMicro-confocal (Molecular Devices, USA) equipped with 4x S Fluor lens in two channels: filter set DAPI (ex 377 nm/em 447 nm) and FITC (ex 475 nm/em 536 nm) for total cells and infected cells, respectively.

Images were analyzed using MetaXpress CME (Molecular Devices) to quantify the number of total and infected cells. Settings for segmentation: cell/nuclei size 5-30 µm and intensity >2000AU.

The inhibition % was calculated accordingly to:

$$\text{Inhibition \%} = \left\{ 1 - \frac{I_{Compound}}{(I_{max} - I_{min})} \right\} \times 100$$

$I_{Compound}$ = Number of infected cells in presence of compounds.
I_{max} = Number of infected cells in absence of compounds.
I_{min} = Number of infected cells in absence of viruses.

Dose response assay

For dose-response assay the compounds were serially diluted to cover a range of 40-0.31 µM. The assay is identical to phenotypic assay as described above. Six different VSVΔG viruses representing G, WT, Alpha, Delta, Omicron, and MERS were tested. Data were deposited in Collaborative Drug Discovery platform (CDD vault; Collaborative Drug Discovery, USA), and dose response curves were analyzed from image analysis. Dose response curves were generated and fitted to the Levenberg–Marquardt algorithm that is used to fit a Hill equation to dose-response data.

Cell viability assay

To assess compounds toxicity to cells, a copy of the compound as in dose-response experiment were assayed for cell viability assay. Cells were stained with Hoechst 33342 in addition to 1.5 µM Propidium Iodide (Life Technologies, USA) and 2 µM Calcein AM (Life Technologies). Images were then captured using the ImageXpressMicro-confocal, and analysis was performed by MetaXpress CME adjusted to quantify total, live or dead cells.

Spike-ACE2 binding assay

To test if the compounds inhibited S1-domain and ACE2 interactions, a commercial ELISA kit (SARS-CoV-2 Spike S1 RBD: ACE2 Inhibitor Screening Assay Kit; BPS Bioscience, USA) was used according to the manufacturer's protocol. The compounds were tested in triplicates

with serial dilutions covering a range of 10-0.01 μM, while the positive control, soluble Spike was tested in serial dilutions covering a range of 0.7-0.001 μM. The soluble Spike was produced from a plasmid[69] obtained from Florian Krammer (Icahn School of Medicine, Mt. Sinai, USA) by The Dana and Yossie Hollander Center for Structural Proteomics, Weizmann Institute of Science.

All the reagents were used from the kit. Briefly, a 96-well nickel-coated plate was coated with ACE2-His and incubated for 60 min before washing. The plate was then incubated with a blocking buffer for 10 mins and removed. Next, the compounds or soluble Spike were added and incubated for 60 min at room temperature with slow shaking. Following incubation, SARS-CoV-2 Spike (RBD)-Fc was added into all wells except for the blank, and the plate was left to sit with slow shaking. After 60 min, an anti-mouse Fc-HRP anitbody was added, followed by the addition of an Enhanced chemiluminescence (ECL) solution to produce chemiluminescence. Finally, a Cytation 5 plate reader (BioTek, USA) was used to read and quantify the luminescence. The final concentration of DMSO was 5% in each wells.

Liquid chromatography-mass spectrometry (LC/MS)

Flash chromatography was first performed by automated CombiFlash Systems (Teledyne ISCO, USA) with RediSep Rf Normal-phase silica gel columns (Teledyne ISCO) or Silica gel Kieselgel 60 (0.04-0.06 mm) columns (Merck, USA). Purification of the compounds was then performed using preparative HPLC; Waters Prep 2545 Preparative Chromatography System (Waters, USA), with 2489 UV/Vis detector (Waters), using XBridge HPLC Column (Waters). Compounds purity was monitored by UPLC-MS system: Acquity UPLC H class with PDA detector and ELSD detector (Waters) and using Acquity UPLC BEH C18 Column (Waters). MS-system: SQ detector 2 (Waters). UPLC Method using HPLC grade solvents: 5 min gradient 95:5 Water (Merck): Acetonitrile (Merck) 0.05% formic acid (Bio-lab, Israel) to Acetonitrile 0.05% formic acid, flowrate 0.5 mL/min, column temp 40°C.

Synthesis of PCM-0163855 and PCM-0282478

All reagents, solvents and building blocks used for synthesis without further purification. All solvents used for reactions were of HPLC grade. Solvent and reagent abbreviations: Ethyl acetate (EtOAc; Bio-lab), Dichlormethane (DCM; Bio-Lab), Dimethylformamide (DMF, Sigma Aldrich), Tetrahydrofuran (THF; Sigma Aldrich), Acetonitrile (MeCN; Bio-Lab), 1,8-Diazabicyclo[5.4.0]undec-7-ene (DBU; Sigma Aldrich), Diisopropylethyl amine (DIPEA; Sigma Aldrich), Trifluoroacetic acid (TFA; Sigma Aldrich), Sodium sulfate (Na_2SO_4; Sigma Aldrich), Lithium hydroxide (LiOH; Sigma Aldrich), Hydrochloric acid (HCl; Bio-lab), Hexafluorophosphate azabenzotriazole tetramethyl uronium (HATU; Sigma Aldrich), meta-Chloroperoxybenzoic acid (mCPBA; Sigma Aldrich), Sodium sulfite (Na_2SO_3; Sigma Aldrich)

Reactions on microwave were done on Initiator+ (Biotage, Sweden). ^{1}H NMR spectra were recorded on an Avance III (Bruker, USA) - 300 MHz, 400 MHz and 500 MHz spectrometer, equipped with QNP probe. Chemical shifts are reported in ppm on the δ scale and are calibrated according to the deuterated solvents. All J values are given in Hertz.

Ethyl 2-((1-(4-chlorophenyl)-4-phenyl-1H-imidazol-2-yl)thio)acetate (2): To a 5 mL crimp vial, ethyl bromo acetate (87.3 mg, 0.52 mmol; Sigma Aldrich) was added followed by 1-(4-chlorophenyl)-4-phenyl-1H-imidazole-2-thiol (1)[70] (100.0 mg, 0.35 mmol) and DIPEA (182.0 μl, 1.05 mmol). The vial was crimped and heated at 90 °C for 5min in microwave reactor, and the reaction was cooled and diluted with EtOAc (10 ml), the organic layer was washed 1X water, 1X brine (Sigma Aldrich) and dried on Na_2SO_4. The organic layer was concentrated onto 0.5 g silica (Sigma Aldrich) and purified on a Combi-Flash Systems, using a 24 g silica gel column gradient (15 min) from DCM to EtOAc. The fraction that eluted in 50% EtOAc gave compound 2 (123.0 mg, 94 % yield).

2-((1-(4-chlorophenyl)-4-phenyl-1H-imidazol-2-yl)thio)acetic acid (3): Compound 2 (123.0 mg, 0.33 mmol) was dissolved in THF (2 ml), then LiOH (197.0 mg, 8.24 mmol) was dissolved in water (2 ml), and the freshly prepared solution was added to the reaction and stirred overnight. The reaction mixture was cooled to 0 °C and acidified to pH = 4 with HCl 1M (∼ 9 ml), the aqueous layer was extracted 3x EtOAc, the combined organic layers were washed with brine dried on Na_2SO_4. The organic layer was concentrated to give compound 3 (106.2 mg, 93% yield).

2-((1-(4-chlorophenyl)-4-phenyl-1H-imidazol-2-yl)thio)-N-(2,3-dimethylphenyl)acetamide (4): In a 25 mL round bottom flask, compound 3 (106.0 mg, 0.31 mmol) and 2,3-dimethylaniline (72.7 mg, 0.46 mmol) was dissolved in DMF (2 ml). Then DIPEA (214.0 μl, 1.23 mmol) was added followed by HATU (128.6 mg, 0.34 mmol) and the reaction was stirred for 12h. The reaction was then poured into brine (10 ml) and the aqueous layer was extracted 3 X EtOAc, the combined organic layer was washed with 1x water, 1x brine and dried on Na_2SO_4. The organic layer was concentrated onto 0.5 g silica and purified on Combi-Flash Systems, using a 24 g silica gel column gradient (17 min) from DCM to EtOAc, the fraction that eluted in 50% EtOAc gave compound 4 (108.2 mg, 79% yield).

2-((1-(4-chlorophenyl)-4-phenyl-1H-imidazol-2-yl)sulfonyl)-N-(2,3-dimethylphenyl)acetamide (PCM-0163855): To a 25 mL round bottom flask, compound 4 (19.5 mg, 0.044 mmol) was dissolved in DCM (2 ml), then mCPBA (24.4 mg, 0.11 mmol) was added in one portion. After 2h an additional amount of mCPBA (10 mg) was added and the reaction was stirred overnight. The reaction mixture was quenched with Na_2SO_3 (30 μl) and concentrated on rotary evaporator. Purification of the crude reaction mixture by HPLC water to MeCN gradient 45 min, the desired compound eluted in 80% MeCN to give **PCM-0163855** (13.5 mg, 62% yield). 1H-NMR (300 MHz, DMSO-d6) δ 9.82 (s, 1H), 8.22 (s, 1H), 7.88 (d, 2H, J = 8 Hz), 7.60-7.50 (m, 4H), 7.48-7.40 (m, 2H), 7.37-7.29 (m, 1H), 7.08-7.00 (m, 3H), 4.67 (s, 2H), 2.24 (s, 3H), 1.97 (s, 3H); ES-LRMS: (*m/z*) calculated for $C_{25}H_{23}ClN_3O_3S$ ([M+H]+) 480.1, found 480.3.

2-((1-(4-chlorophenyl)-4-phenyl-1H-imidazol-2-yl)sulfinyl)-N-(2,3-dimethylphenyl)acetamide (PCM-0282478): To a 25 ml round bottom flask, compound 4 (52.0 mg, 0.012 mmol) was dissolved in DCM (2 ml), then mCPBA (28.6 mg, 0.013 mmol) was added in one portion and the reaction was stirred overnight. The reaction mixture was quenched with Na_2SO_3 (30 μl) and the reaction was concentrated on rotary evaporator. Purification of the crude reaction mixture by HPLC water to MeCN gradient 45 min, the desired compound eluted in 80% MeCN to give PCM-0282478 (35.1 mg, 65% yield). Chiral Separation was performed at Lotus Separations (USA, http://lotussep.com/). 1H-NMR (300 MHz,

DMSO-d6) δ 10.02 (s, 1H), 8.31 (s, 1H), 7.95 (d, 2H, J=7.5 Hz), 7.78-7.68 (m, 4H), 7.51-7.41 (m, 2H), 7.38-7.30 (m, 1H), 7.06-6.98 (m, 3H), 4.98 (d, 1H, J=14 Hz), 4.64 (d, 1H, J=14 Hz), 2.21 (s, 3H), 1.96 (s, 3H); (ES-LRMS: (m/z) calculated for $C_{25}H_{23}ClN_3O_2S$ ([M+H]+) 464.1, found 464.3.

SARS-CoV-2 replication assay

Clear-bottomed 384-well black plates were seeded with 3,000 Vero E6 cells or Vero E6-TMPRSS2 cells per well. The following day, individual compounds were added at ten specified concentrations, 2 h prior to infection. Each plate included 0.5 % DMSO and 25 μM Remdesivir (Selleck Chemicals) controls. After the pre-incubation period, the cells were exposed to the Delta B.1.617.2 inoculum (at a multiplicity of infection of 0.05 PFU/Vero E6 cell and 0.2 PFU/Vero TMPRSS2 cell). After a one-hour adsorption at 37°C, the supernatant was aspirated and replaced with 2% FBS/DMEM media containing the respective compounds at the indicated concentrations. The cells were then incubated at 37 °C for 2 days. Supernatants were collected and heat inactivated at 80 °C for 20 minutes. The Luna Universal One-Step RT-qPCR Kit (New England Biolabs, USA) was used for the detection of viral genomes in the heat-inactivated samples performed through reverse transcription quantitative polymerase chain reaction (RT-qPCR). Specific primers targeting the N gene region of SARS-CoV-2 (5′-TAATCAGACAAGGAACT GATTA-3′ and 5′-CGAAGGTGTGACTTCCATG-3′) were utilized. The cycling conditions involved an initial step at 55 °C for 10 minutes, followed by 95 °C for 1 minute. Subsequently, 40 cycles were carried out with denaturation at 95 °C for 10 seconds and annealing/extension at 60 °C for 1 minute using an QuantStudio 6 thermocycler (Applied Biosystems, USA). The quantity of viral genomes is expressed as Ct and was normalized against the Ct values of the negative and positive controls.

In parallel, cytotoxicity was assessed using the CellTiter-Glo luminescent cell viability kit (Promega, USA). 3,000 cells/well of Vero E6 were seeded in white with clear bottom 384-well plates. The following day, compounds were added at concentrations indicated. 0.5% DMSO and 10 μM Camptothecin (Sigma Aldrich) controls were added in each plate. After 48 h incubation, 10 μl of CellTiter Glo reagent was added in each well and the luminescence was recorded using a luminometer (Berthold Technologies, Germany) with 0.5 sec integration time.

Raw data were normalized against appropriate negative (0 %) and positive controls (100 %) and are expressed in % of viral replication inhibition or % of cytotoxicity. Curve fits and IC_{50}/CC_{50} values were obtained in Prism (GraphPad, USA) using the variable Hill slope model.

SARS-CoV-2 plaque assay

Plaque assay was performed to determine the viral load of *bona fide* SARS-COV-2 Delta variant with a dose-response of two enantiomers of PCM0282478 (in duplicates). Vero E6 cells were seeded in 24-well plates at a concentration of 7.5×10^4 cells per well. The following day, serial dilutions of each supernatant were performed in serum-free DMEM medium. After 1 h absorption at 37 °C, 2× overlay medium was added to the inoculum to give a final concentration of 2% (v/v) FBS in DMEM and 0.4% (w/v) agarose (Sigma Aldrich) to achieve a semi-solid overlay. Plaque assays were incubated at 37 °C for 3 days. Samples were fixed using 4% formaldehyde solution and plaques were visualized using crystal violet solution (Merck). To calculate the plaque forming units (PFU) per well, counts from duplicate wells were averaged, and the average was multiplied by the dilution factor and the volume of inoculum plated. The calculation is: the average value of plaques in duplicate wells × dilution factor ÷ virus inoculum volume (in μL) x volume per well = titer in PFU/well.

QUANTIFICATION AND STATISTICAL ANALYSIS

Statistical analysis and tools

Data from analyzed images was processed using Genedata Screener (Genedata, Switzerland). Normalization was the percent of infection where neutral control is 0% inhibition of infection and "No-Virus" control is 100% inhibition of infection. Further chemoinformatic data visualizations were made with D360 software (Certara, USA), which is integrated with the CDD vault. Excel (Microsoft, USA) was used to analyze the data and Prism was used to plot the data. Whenever comparing between two conditions, data was analyzed with two tailed student's t-test. Measurements are reported as mean of at least three biological repeats, and the error bars denote standard error of mean (SEM). Throughout the study, threshold for statistical significance was considered for p-values ≤ 0.05, denoted by one asterisk (*), two (**) if P ≤ 0.01, three (***) if P < 0.001 and four (****) if P ≤ 0.001.